The Astrophysical Journal Supplement Series, 262:26 (26pp), 2022 September https://doi.org/10.3847/1538-4365/ac7ffe

The Formation of the Stripped-envelope Type IIb Supernova Progenitors: Rotation, Metallicity, and Overshooting

Gang Long[1], Hanfeng Song[1,2], Georges Meynet[2], Andre Maeder[2], Ruiyu Zhang[3], Ying Qin[4], Sylvia Ekström[2], Cyril Georgy[2], and Liuyan Zhao[1]
[1] College of Physics, Guizhou University, Guiyang City, Guizhou Province, 550025, People's Republic of China; hfsong@gzu.edu.cn
[2] Geneva Observatory, Geneva University, CH-1290 Sauverny, Switzerland; Georges.Meynet@unige.ch, Andre.Maeder@unige.ch
[3] College of Physics, Henan Normal University, Xinxiang, Henan Province, 453007, People's Republic of China
[4] Department of Physics, Anhui Normal University, Wuhu City, Anhui Province, 241000, People's Republic of China
Received 2022 March 14; revised 2022 June 13; accepted 2022 July 7; published 2022 September 2

Abstract

Type IIb supernovae (SNe) are believed to originate from core-collapse progenitors having kept only a very thin hydrogen envelope. We aim to explore how some physical factors, such as rotation, metallicity, overshooting, and the initial orbital period in binaries significantly affect the Roche lobe overflow and the formation of Type IIb SNe (also denoted SNe IIb). It is found that binaries are the main channel that are capable of producing Type IIb SNe progenitors in the mass range for initial masses below $20\,M_{\odot}$. The formation of Type IIb SNe progenitors is extremely sensitive to the initial orbital period. A less massive hydrogen envelope mass indicates a smaller radius and higher effective temperatures, and vice versa. Binary systems with initial periods between 300 and 720 days produce Type IIb progenitors that are a red supergiant. Those with an initial period between 50 and 300 days produce yellow supergiant progenitors, and those with initial periods shorter than 50 days blue supergiant progenitors. Both rapid rotation and larger overshooting can enlarge the carbon–oxygen core mass and lead to higher core temperature and lower central density at the precollapse phase. They are also beneficial to surface nitrogen enrichment but restrict the efficiency of the first dredge-up. SN IIb progenitors with low metallicity have smaller hydrogen envelope masses and radii than their high-metallicity counterparts. Ultrastripped binary models have systematically higher core mass fraction ^{12}C left, which has an important influence on the compactness of Type IIb progenitors.

Unified Astronomy Thesaurus concepts: Close binary stars (254); Stellar rotation (1629); Massive stars (732); Stellar structures (1631); Stellar properties (1624)

1. Introduction

Massive stars explode as core-collapse supernovae (SNe) with varying amounts of hydrogen in their envelopes. SNe are classified as Type I and Type II in terms of the absence and presence of H lines in their spectra and further subdivided into types Ia, Ib, Ic, IIP, IIL, IIb, and IIn (e.g., Branch et al. 1991; Filippenko 1991). The spectra of Type I core-collapse SNe show an absence of H lines. The presence of strong silicon (Si) lines and helium (He) lines defines Type Ia and Type Ib, respectively, while Type Ic do not display any H and He features in their spectra. There are a few signatures of H in the spectra of Type Ib SNe.

It has been suggested that the diversity of Type II SNe originates from the different main-sequence mass ranges of the progenitors, i.e., SNe IIL being from about 7 to $10\,M_{\odot}$, SNe IIP being above $10\,M_{\odot}$, and SNe Ib/Ic originating from He stars of different mass ranges in binary systems (Nomoto et al. 1990). However, the exact connection of these types to their progenitors has been a controversial issue.

In this paper, we focus on stripped-envelope (SE) SNe, e.g., SNe of types IIb, Ib, and Ic. Type IIb SNe are considered as a transitional class, showing clear hydrogen signatures in their early spectra. However, these signatures gradually disappear over a period 30–90 days after explosion, after which the spectra become virtually indistinguishable from Type Ib SNe. Possibly the simplest explanation for these observational differences among the SE SNe subclasses is that different amounts of the helium/hydrogen envelopes have been stripped from the star prior to the SN explosions. In this channel, Type Ic SNe are stripped the most whereas Type IIb are the least.

The light curves of SNe IIb can show an early fireball phase but are powered near maximum and beyond by radioactive decay. The thin envelope model has been confirmed by spectral variations, which show growing features of helium and oxygen. The light curves of SNe IIb are significantly different from the previously known light curves of SNe II. It is obvious that the peculiar light curves of SNe IIb cannot be explained by the explosion of an ordinary red supergiant (RSG) with a massive hydrogen-rich envelope, which produces rather the light curve of an SNe IIP. The light curve of an SNe IIb can be understood as the explosion of an RSG whose hydrogen-rich envelope is as small as $M < 1.0\,M_{\odot}$. For example, SN 1993J in M81 has been identified as a Type IIb (Schmidt et al. 1993). This behavior implies that the progenitor of the core collapse has a very small hydrogen mass at the time of explosion, $M_{\rm H} \simeq 0.03-0.5\,M_{\odot}$ (e.g., Woosley et al. 1994; Meynet et al. 2015; Yoon et al. 2017), with a possible mass down to $M_{\rm H} \simeq 0.001\,M_{\odot}$ (Eggleton 1983; Dessart et al. 2011). In a population synthesis investigation, Sravan et al. (2018) considered the mass of the hydrogen-rich envelope of the progenitor at the onset of explosion to be $0.01\,M_{\odot} \leqslant M_{\rm H} \leqslant 1.0\,M_{\odot}$.

However, the mechanisms driving the stripping of the hydrogen envelope and the parameter regimes that dominate

the formation of SNe IIb are still open questions. Two physical mechanisms for envelope removal have been proposed to explain the progenitors of SNe IIb. In the first scenario, a very massive star with initial mass ($>25\,M_{\odot}$) is required in order for the mass-loss rate to be large enough (e.g., Woosley et al. 1993; Heger et al. 2003) and at sufficiently high initial metallicity for stellar winds to be triggered. This scenario is supported by the analysis of the environments of Type Ib/c SNe, in which very massive stars ($\geqslant 30\ M_{\odot}$) have lost their envelopes through stellar winds (Maund 2018). In order to meet with the complete set of observations of SN 2008ax, Georgy (2012) constructed a Type IIb progenitor of $20\,M_{\odot}$ ending with the suitable core mass, color, luminosity, and hydrogen content. Groh et al. (2013) displayed the final stage of the rotating model as a luminous blue variable (LBV) star and proposed that LBVs may be the progenitors of some core-collapse SNe. However, the observed SE SN rates are too high to be explained solely by single-star evolution. The biggest difficulty with the single-star scenario is that the evolution of a single star requires extremely precise fine tuning of the initial parameters to leave a thin hydrogen envelope prior to the explosion. Moreover, the clumping in stellar winds suggests that the currently used mass-loss rates are too high for single-star evolution; the hot wind mass-loss rates are lower by a factor of 2 or 3 than those typically used in stellar evolution calculations. The lower wind-loss rate makes it difficult to produce SNe IIb by single-star evolution.

The second scenario is close binary interactions involving mass transfer via the Roche lobe overflow (RLOF) and possibly common envelope evolution (CEE; e.g., Podsiadlowski et al. 1992; Nomoto et al. 1993; Podsiadlowski et al. 1993; Yoon et al. 2010, 2017), stellar evolution with rotation (e.g., Georgy 2012; Groh et al. 2013), and nuclear-burning instabilities (e.g., Arnett & Meakin 2011; Strotjohann et al. 2015). Joss et al. (1988) showed that binary evolution can produce stripped supergiants with small hydrogen-rich envelopes. The typical ejecta mass of SE SNe may be very low ($\sim$2–4 $M_{\odot}$), indicating that the progenitors originated from lower mass stars ($\leqslant 20\ M_{\odot}$) that have lost their envelopes through binary interaction (Lyman et al. 2016; Taddia et al. 2018; Prentice et al. 2019). Claeys et al. (2011) identified binary progenitor models for extended Type IIb SNe. The hydrogen envelope of the primary star is stripped by the RLOF and only several tenths of the solar mass of the hydrogen envelope can remain at the time of explosion.

The most direct way to distinguish between these scenarios is to search for a surviving binary companion after the SNe. Such searches have been successful for Type IIb SNe, where putative surviving companions have been discovered, e.g., SN 1993J (Maund et al. 2004), SN 2011dh (Folatelli et al. 2014; Maund 2019), and SN 2001ig (Ryder et al. 2018). These findings are very important indicators which originate from binary systems. Torrey et al. (2019) presented an enhanced-mass-loss scenario due to jets possibly driven by the companion star, and noted that enhanced mass loss can cause the binary system to go through grazing envelope evolution (GEE) and generate a progenitor of Type IIb SNe. They estimated that the binary evolution channel with GEE contributes about a quarter of all SNe IIb. The GEE channel is completely different from the RLOF scenario, and hence widens the binary parameter space that can account for Type IIb SNe. The fatal CEE scenario can also produce some SNe IIb: a lower mass main-sequence companion star circles inside the giant envelope of the primary star and eliminates most of the giant envelope before it merges with the giant core. However, this channel is confronted with some uncertainties in the calculations (Soker 2017; Lohev et al. 2019).

Close binary stars are important in understanding the formation, evolution, and death of massive stars. A high fraction of O-type stars (70%) at solar metallicity are expected to undergo a mass-transfer episode during their lifetime (Sana et al. 2012). There is some evidence for two subclasses of SNe IIb, those with radially extended hydrogen envelopes and those with compact envelopes (Chevalier & Soderberg 2010). Yoon et al. (2017) investigated the formation of SNe IIb in the channel of mass transfer via RLOF while considering three groups of SNe IIb, namely blue progenitors, yellow supergiants (YSGs), and RSGs. The more compact blue progenitors and YSGs have hydrogen envelope masses less than about $M_{\rm H} < 0.15\,M_{\odot}$, mostly resulting from early Case B mass transfer with relatively low initial masses and/or low metallicity. RSGs have hydrogen masses $M_{\rm H} > 0.15\,M_{\odot}$ at explosion, which can be produced via late Case B mass transfers.

In this paper, we intend to explore the role of the close binary evolution scenario in producing the SNe IIb. We aim to explore the following questions in the binary scenario: (1) how do some initial physical parameters (i.e., rotational velocities, overshooting, metallicity, and orbital period) impact on the formation of SNe IIb; (2) how does the surface chemical abundance vary with these initial parameters; (3) what controls the mass of the hydrogen-rich envelope of the progenitor through mass transfer due to RLOF; (4) what is the relation between SNe IIb and other types of SNe, such as SNe IIP, IIL, and Ib/c; and (5) how the internal structure of the deep core is influenced by these initial parameters.

In Section 2, we describe the physical ingredients of the stellar models and the domains of initial conditions that we explore in this work. In Section 3, the results of numerical calculations for the evolution of single stars and binary systems are presented in detail. In Section 4, we discuss an unsolved, long-standing problem about the discrepancy between the observed ratio of Type IIb SNe and the theoretical one. Conclusions and summaries are given in Section 5.

2. The Initial Parameters and Model Descriptions

All models are calculated with the MESA code (Paxton et al. 2011, 2013, 2015, 2018). We make use of the Schwarzschild criterion to determine the boundaries of the convective region. The mixing length parameter is $l_{\rm m} = 1.5\,H_{\rm P}$, where $H_{\rm P}$ is the pressure scale height at the outer boundary of the core. We consider an overshoot parameter of 0.12 $H_{\rm P}$ as the reference value. Sravan et al. (2020) have shown that SN 2013df and SN 1993J have very low mass limits (about 2.0–2.8 $M_{\odot}$) of helium cores. This fact makes a smaller overshoot parameter a more appropriate choice; a smaller overshoot parameter can also be supported from intermediate-mass eclipsing binaries (Stancliffe et al. 2015). Normally, a standard value of the overshoot parameter is 0.25 $H_{\rm P}$. Brott et al. (2011) considered convective overshooting using a parameter of 0.335 $H_{\rm P}$. This value results from their new calibration using the observed $v\sin(i)$ drop that is found in their data when they plot $v\sin(i)$ against the surface gravity. We assume that the helium abundance increases linearly from $Y = 0.2477$ (Peimbert et al. 2007) at $Z = 0.0$ to

Table 1
The Parameters Adopted in Our Calculations

Models	$M_{1,\mathrm{ini}}$ ($M_\odot$)	$M_{2,\mathrm{ini}}$ ($M_\odot$)	$V_{1,\mathrm{ini}}$ (km s^{-1})	$V_{2,\mathrm{ini}}$ (km s^{-1})	$P_{\mathrm{orb,ini}}$ (days)	α_{over}	Z	M_{He} ($M_\odot$)	M_{H} ($M_\odot$)	$R/R_\odot$	ST	SP
S1	15	⋯	0	⋯	⋯	0.12	0.02	4.34	8.60	741	IIP	RSG
S2	15	⋯	200	⋯	⋯	0.12	0.02	4.40	7.62	812	IIP	RSG
S3	15	⋯	400	⋯	⋯	0.12	0.02	5.87	3.52	1023	IIP	RSG
S4	17	⋯	0	⋯	⋯	0.12	0.02	5.19	8.16	950	IIP	RSG
S5	17	⋯	200	⋯	⋯	0.12	0.02	5.21	8.02	948	IIP	RSG
S6	17	⋯	400	⋯	⋯	0.12	0.02	6.38	3.67	891	IIP	RSG
S7	19	⋯	0	⋯	⋯	0.12	0.02	6.00	9.00	1047	IIP	RSG
S8	19	⋯	200	⋯	⋯	0.12	0.02	5.92	8.11	1061	IIP	RSG
S9	19	⋯	400	⋯	⋯	0.12	0.02	7.30	3.13	851	IIP	RSG
B1	17	15	0	0	300.00	0.12	0.02	4.81	0.35	478	IIb	RSG
B2	17	15	0	0	300.00	0.25	0.02	5.61	0.3	407	IIb	YSG
B3	17	15	0	0	300.00	0.35	0.02	5.44	0.0	2	Ib	WR
B4	17	15	0	0	300.00	0.12	0.008	5.54	0.46	512	IIb	RSG
B5	17	15	0	0	300.00	0.12	0.03	5.00	0.27	436	IIb	YSG
B6	17	15	0	0	3.00	0.12	0.02	3.34	0.0	6	Ib	WR
B7	17	15	0	0	10.00	0.12	0.02	4.60	0.14	14	IIb	BSG
B8	17	15	0	0	700.00	0.12	0.02	4.94	0.49	549	IIb	RSG
B9	17	15	0	0	1600.00	0.12	0.02	4.95	1.88	891	IIP	RSG
B10	17	15	200	200	300.00	0.12	0.02	4.81	0.35	331	IIb	YSG
B11	17	15	400	400	300.00	0.12	0.02	4.81	0.35	2	Ib	WR
B12	17	15	0	0	50.00	0.12	0.02	4.63	0.14	166	IIb	BSG
B13	16	15	0	0	1100.00	0.12	0.04	5.01	0.39	565	IIb	RSG

Note. The meaning of each column is as follows. The symbol "S" denotes single stars whereas the symbol "B" denotes binary systems. $M_{1,\mathrm{ini}}$: the initial mass of the primary star; $M_{2,\mathrm{ini}}$: the initial mass of the secondary star; $V_{1,\mathrm{ini}}$: the initial equatorial velocity of the primary star; $V_{2,\mathrm{ini}}$: the initial equatorial velocity of the secondary star; $P_{\mathrm{orb,ini}}$: the initial orbital period; α_{over}: the convective overshoot parameter; Z: metallicity; M_{He}: the mass of the helium core at core carbon exhaustion; M_{H}: the mass of the hydrogen envelope at core carbon exhaustion. ST: Supernovae type. SP: the type of supernovae progenitor.

$Y = 0.28$ at $Z = 0.02$ (Brott et al. 2011). We adopt the basic.net, coburn.net, and approx21.net nuclear networks in MESA.

Our models are comprised of single or two zero-age main-sequence (ZAMS) stars; their various initial parameters are listed in Table 1. In order to conform with observations of two component stars of SN 1993J in the Hertzsprung–Russell (HR) diagram, the accretion efficiency β_{mt}, (i.e., the fraction of transferred material that is accreted by the companion star) is then chosen as $\beta_{mt} = 0.5$. The final hydrogen envelope mass increases if we employ a lower accretion efficiency. For a higher accretion efficiency, the secondary star tends to evolve toward an overluminous O-type star. The nonaccreted matter is directly expelled from the system as a fast wind for the accretor and carries the specific orbital angular momentum of the mass gainer. We use the Dutch scheme in MESA for both hot and cool wind mass-loss rates, with a Dutch scaling factor of 1.0.[5] The wind of Wolf–Rayet (WR) stars is computed according to Nugis & Lamers (2000). Radiative opacities were interpolated from OPAL tables (Iglesias & Rogers 1996). The opacity increase due to Fe-group elements at $T \sim 180$ kK plays an important role in determining the envelope structure in our stellar models.

We take into account various instabilities induced by rotation that result in the mixing of chemical elements: Eddington–Sweet circulation, dynamical and secular shear instability, and the Goldreich–Schubert–Fricke instability (Endal & Sofia 1978; Pinsonneault et al. 1989; Maeder & Meynet 2000b, 2012). The rotational mixing owing to these hydrodynamic instabilities is considered as diffusion processes according to Heger et al. (2000). The diffusion coefficients are adopted for the transportation of both chemical species and angular momentum. The contribution of the rotationally induced instabilities to the total diffusion coefficient of the chemical species is decreased by the parameter $f_c = 0.0228$. This factor has been calibrated to reproduce the observed nitrogen surface abundances as a function of the projected rotational velocities for stars in the Large Magellanic Cloud sample (NGC 2004) of the FLAMES survey (Brott et al. 2011). The parameter f_μ denotes the sensitivity of the rotationally induced mixing to mean molecular weight gradients (i.e., the mean molecular weight gradients ∇_μ is replaced by $f_\mu \nabla_\mu$; Heger et al. 2000). We adopt a value $f_\mu = 0.1$ as in Yoon et al. (2006), who calibrated this parameter to match the observed surface helium abundances in stellar models with solar metallicity.

The upper mass limit of the hydrogen envelope for SNe IIb depends heavily on the SN parameters, such as chemical composition, total mass of ejecta, and SN energy. We assume that models with final hydrogen-rich envelope masses of more than $0.5\,M_\odot$ explode as SNe IIP or SNe IIL, while those with envelope masses less than $0.033\,M_\odot$ explode as SNe Ib or Ic. Models whose envelope mass is between $0.033\,M_\odot$ and $0.5\,M_\odot$ are adopted as SN IIb progenitors. The properties of the SN IIb progenitor are also shown in Table 1. The final evolutionary positions in the HR diagram are classified according to their effective surface temperature and surface hydrogen mass fraction, as follows: red supergiant (RSG): $T_{\mathrm{eff}} < 4.8$ kK, $X_s \geqslant 0.01$; yellow supergiant (YSG): $4.8\,\mathrm{kK} < T_{\mathrm{eff}} < 7.5$ kK, $X_s \geqslant 0.01$; blue supergiant (BSG): $7.5\,\mathrm{kK} < T_{\mathrm{eff}} < 55$ kK, $X_s \geqslant 0.01$; hot helium giant: $15\,\mathrm{kK} < T_{\mathrm{eff}} < 55$ kK, $X_s < 0.01$;

[5] The Dutch wind mass-loss scheme is a combination of the prescriptions of Vink et al. (2001; when $T_{\mathrm{eff}} \geqslant 10^4$ K and $X_{\mathrm{surf}} \geqslant 0.4$), Nugis & Lamers (2000; when $T_{\mathrm{eff}} \geqslant 10^4$ K and $X_{\mathrm{surf}} < 0.4$), and de Jager et al. (1988; when $T_{\mathrm{eff}} < 10^4$ K).

cool helium giant: $T_{\rm eff} < 15$ kK, $X_s < 0.01$; WR star: 10 kK $< T_{\rm eff} <$ 251 kK, $X_s \leqslant 0.4$ (Gilkis & Arcavi 2022).

The initial parameters for single stars and the binary system are listed in Table 1. The binary orbit is assumed to be circular and the Roche lobe radius is given by the formula of Eggleton (1983). The mass ratio is set to be $q = 0.882$ for all binary models. In the systems with $q = \frac{M2}{M2} < 0.7$–0.8, relying on the orbital period, the mass-transfer rate via RLOF is so large that two component stars come into contact. Further CEE of these models requires complex considerations which are beyond the scope of this paper. In fact, binary systems with lower mass ratios have issues in explaining SNe IIb, in particular those with extended hydrogen envelopes with $M_H > 0.15\,M_\odot$ (Podsiadlowski et al. 1992). We choose several initial orbital periods corresponding to cases where the first mass-transfer event occurs during the main-sequence phase ($P_{\rm orb} = 3.0$ days; Case A), after core hydrogen exhaustion but before the helium ignition in the core ($P_{\rm orb} = 10.0$ days; Case B), and during the core helium-burning phase ($P_{\rm orb} > \sim 40.0$ days; Case C).

3. Results of Numerical Calculations

We present nonrotating and rotating single-star models and compare them with binary models with various initial parameters. We focus our investigation on the evolution of the primary star and explore whether close binary evolution via different initial orbital periods (i.e., Case A, Case B, or Case C mass transfer), overshoot parameters, and metallicities could give rise to diverse SNe IIb in terms of the amount of the removed hydrogen or helium envelope. The evolution of the close binary system composed of a 17 $M_\odot$ primary star and a 15 $M_\odot$ companion star is computed. In all models, we calculate the evolution at least to the end of central neon burning.

The properties of single stars and the primary star in binaries, such as evolutionary age, actual mass, radius, effective temperature, luminosity, central temperature and central density; the ratio of the surface nitrogen to the initial value; equatorial velocities; the mass fractions of chemical elements such as surface mass fraction of hydrogen and helium, as well as the logarithms of mass fraction of surface chemical elements such as carbon, nitrogen and oxygen; and the mass ratio of the surface nitrogen to carbon are presented in Table 3.

3.1. The Evolution of the Hydrogen Envelope Mass and Surface Nitrogen Enrichments

3.1.1. The Effect of Rotation

Figure 1(a) shows the mass of the hydrogen envelope for single stars with $Z = 0.02$ but with different initial masses and rotational velocities as a function of the evolutionary age. It can be seen that the more massive star has a thicker hydrogen envelope at the end of the core hydrogen-burning phase. For example, the mass of the hydrogen envelope for model S1 with 15.0 $M_\odot$ is 11.38 $M_\odot$ whereas it is 13.38 $M_\odot$ for model S7 with an initial mass 19.0 $M_\odot$. In fact, stellar winds are stronger for more massive stars. The 19.0 $M_\odot$ star loses more than 6 $M_\odot$ while the 15.0 $M_\odot$ counterpart loses less than 4 $M_\odot$. In massive stars, mass loss via stellar winds is mainly a consequence of radiation pressure on atoms during the main-sequence and giant star stages.

The mass loss via stellar winds is proportional to the luminosity of the star and is inversely proportional to its effective temperature during central hydrogen burning. When massive stars evolve toward higher luminosities and lower temperatures, a large fraction of the hydrogen envelope is actually lost by line-driven winds once the central hydrogen has been substantially converted into helium. The mass-loss rates increase when the luminosity increases and hence when the initial mass increases. For an O-type star, the total mass lost by winds during the main sequence is approximately estimated by stellar mass at a power of 2.8 (i.e., $\Delta M \approx M^{2.8}$). These single models undergo dramatic loss of mass on the verge of core hydrogen exhaustion. This is due to the fact that higher luminosity triggers strong mass losses. Moreover, when some stars cross some limit in effective temperature, there is an important change in the ionization structure of the stellar envelope that may produce a great boost in the mass-loss rate due to bistability (Vink et al. 2001).

One can also note that most of the mass is lost during the RSG phase of evolution when the single star burns helium in its core. After the core helium is exhausted, the mass of the envelope changes very little. This is because the evolution proceeds too fast to give rise to a significant mass loss.

Comparing model S4 with $v_{\rm ini} = 0$ km s^{-1} and model S6 with $v_{\rm ini} = 400$ km s^{-1}, one can note that the mass loss is higher for rapidly rotating stars during the main sequence. There are three reasons for this. First, mass loss via stellar winds can also be enhanced by the centrifugal force (Langer 1998). The gravitational acceleration can be significantly reduced by the centrifugal force and the star becomes more expanded. Rotation can also reduce the depth of the gravitational potential, which stellar winds escape from easier, and therefore increases the possibility of the formation of Type IIb SNe at the expense of the RSG stars. However, note that line-driven stellar winds are powered by the radiative flux. This radiative flux is proportional to the effective gravity that decreases when the star is a rapid rotator. This behavior favors the formation of polar winds. However, these effects become much important only at velocities near the critical limit and are likely not important for the models computed here. Second, rotation increases the main-sequence lifetime and thus can allow more time for mass to be lost by stellar winds. Third, rotating stars are more luminous than nonrotating or slower rotating ones and thus they undergo more mass loss by stellar winds. Actually, the rotational mixing is the determining factor here. It changes the track in the HR diagram and causes the star to follow a different mass-loss trajectory. Therefore, rotationally enhanced stellar winds can decrease the minimum mass required for a single star to remove its hydrogen envelope (Meynet & Maeder 2003), thus increasing the generation rate of SN IIb progenitors from single massive stars.

At the end of the evolution, the mass of the hydrogen envelope is thinner in the model with an initial higher velocity. This can be explained by three reasons. First, the convective core can be enlarged greatly by rotational mixing and thus result in a thinner envelope (see Figure 3). Second, rotating stars are more luminous (also in the RSG phase). This enhances the stellar winds during that phase. As a result, the star may evolve away from the RSG region in the HR diagram and become a YSG or even a BSG. Finally, the angular momentum transport efficiency is at a maximum in the convective region due to the largest convective diffusion coefficient.

Figure 2(a) displays the surface mass fraction ratio of nitrogen to carbon for single stars as a function of evolutionary age. There is no surface nitrogen enrichment in the

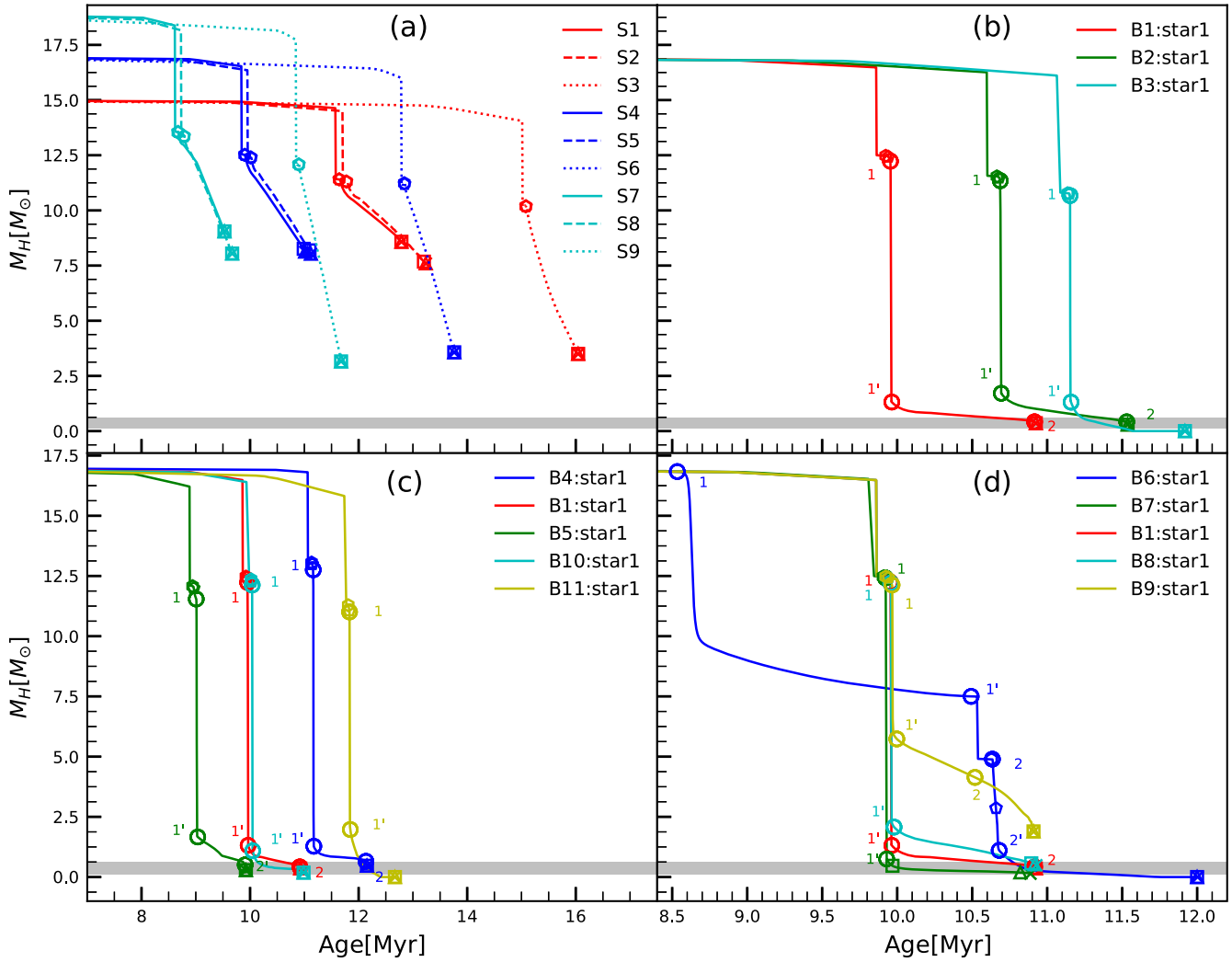

Figure 1. The mass of the hydrogen envelope as a function of evolutionary age. (a) For single stars with various initial masses and rotational velocities. (b) For primary stars with various overshoot parameters in the binary system with initial $P_{\rm orb} = 300$ days. (c) For primary stars with various initial rotational velocities and metallicities in the binary system with initial $P_{\rm orb} = 300$ days. (d) For primary stars in the binary system with various initial orbital periods. Observations for the hydrogen envelope masses of SNe IIb, indicated in shaded regions, are $M_{\rm H} = 0.033$–$0.5\,M_\odot$.

nonrotational models S1, S4, and S7 until the first dredge-up appears. The outer convective region can span a mass coordinate from 16.5 to 4.6 $M_\odot$ during the first dredge-up and may move toward the position of the hydrogen-burning shell. After that, the outer convective envelope shrinks rapidly and develops again from the mass coordinate 13.45 to 5.39 $M_\odot$; it may approach the mass position of the hydrogen-burning shell ($\sim$5.37 $M_\odot$). The carbon–nitrogen–oxygen (CNO) products in the hydrogen-burning shell are mixed by convective dilution. As a result, the surface ratio of nitrogen to carbon increases during the RSG stage.

The nitrogen enrichment for S1, S4, and S7 can also be ascribed to the mass removal of hydrogen envelopes via stellar winds after the main sequence. Markova et al. (2018) noted that the envelope is really stripped in the most luminous supergiants or RSGs by the strong winds ($\log L/L_\odot \geqslant 5.8$ and $\log \dot{M}\,[M_\odot/yr] \geqslant -5.4$). Mass loss may reveal the matter with the enriched nitrogen as the surface matter of the star is peeled. For example, the stellar mass in model S4 reduces from 16.51 $M_\odot$ at the end of hydrogen core burning to 13.45 $M_\odot$ at the end of helium core burning due to the strong RSG stellar winds. A higher ratio of nitrogen to carbon can appear at the surface of more massive stars. This indicates that these two processes are more efficient in more massive stars.

In comparison with the nonrotating counterpart, a significantly higher surface ratio of nitrogen to carbon can be produced by a higher degree of rotational mixing during the main sequence (e.g., Meynet & Maeder 2000; Chieffi & Limongi 2013; Maeder & Meynet 2014; Limongi & Chieffi 2018; Song et al. 2018). The main effect of rotational mixing is to smooth the internal chemical gradients and to facilitate a more progressive arrival of internal nuclear products at the surface (Ekström 2008; Georgy 2012). In MESA massive stars, Eddington–Sweet circulation dominates other rotation-induced instabilities during the main sequence and makes the whole star maintain rigid rotation. In the subsequent evolution, dynamical shear dominates other instabilities in the stellar interior. Maeder et al. (2009) presented results suggesting that the behavior of the surface excess of nitrogen is a multivariate function (i.e., stellar mass, evolutionary age, projected rotational velocity, metallicity) for a single rotating star. As expected, nitrogen enrichment increases with increasing of the initial rotational velocity, initial mass, and evolutionary age during the main sequence due to a higher velocity of the

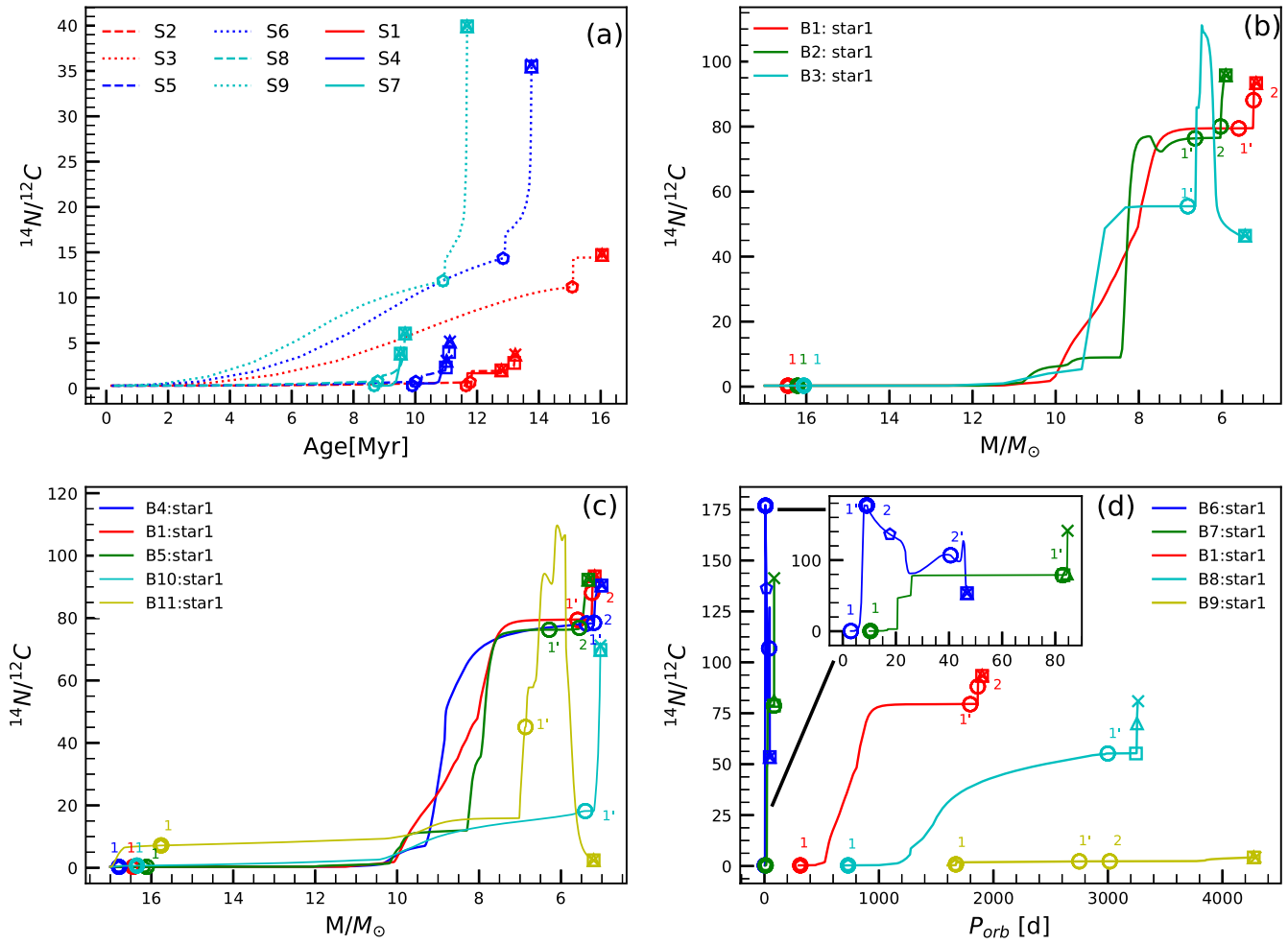

Figure 2. (a) Surface mass fraction ratio of nitrogen to carbon as a function of the evolutionary age for single stars with different initial mass and rotational velocities. (b) This ratio as a function of the actual mass for primary stars with different overshoot parameters in a binary system with an initial $P_{\rm orb} = 300$ days. (c) This ratio as a function of the actual mass for primary stars with different initial metallicities and rotational velocities in a binary system with an initial $P_{\rm orb} = 300$ days. (d) This ratio as a function of the orbital period for primary stars in a binary system with different initial orbital periods.

meridional circulation (see Figure 2(a)). Therefore, rapid rotation can help us explain the nitrogen-rich circumstellar material with a ratio of N/C ≈ 12.4 in SN 1993J. Nitrogen enrichments can be aided by two extra factors. First, strong stellar winds that are enhanced by rotation can remove the hydrogen envelope and expose the hydrogen-burning shell, which is richer in nitrogen. Second, rapid expansion during post-main sequence results in larger differential rotation, which can strengthen the shear instability. Thus the spin angular momentum transportation from the core to the envelope becomes more efficient, meaning that the outer layer can attain a higher rotational velocity, which favors efficient rotational mixing and mass loss by a higher luminosity. For instance, one can notice that the equatorial velocity of the S6 model can attain 144.64 km s^{-1} at the onset of central helium burning (see Table 2). More importantly, the nitrogen enrichment factor N/N_{ini} goes up from 8.49 to 10.02 in model S6 while it rises from 1.0 to 4.34 in model S4 during the first dredge-up. This implies that rotational mixing might reduce the efficiency of the dredge-up due to the decrease in the opacity of the outer envelope. The lower opacity implies a smaller convective envelope, thus reducing the depth of convective dredge-up.

Table 2
Observations of SN 1993J and the Theoretical Values in Models B1 and B13

Observations[a]	Model B1	Model B13
$\log T_{1,\rm eff} = 3.63 \pm 0.05$	3.661	3.63
$\log L_1/L_\odot = 5.1 \pm 0.3$	4.968	4.98
$\log T_{2,\rm eff} = 4.3 \pm 0.1$	4.54	4.39
$\log L_2/L_\odot = 5.0 \pm 0.3$	4.87	4.74
$R/R_\odot \sim 600$	484	565
$\dot{M} \sim 2$–$6 \times 10^{-6}\, M_\odot$ yr^{-1}	$\sim 2.58 \times 10^{-6}\, M_\odot$ yr^{-1}	$\sim 3.0 \times 10^{-6}\, M_\odot$ yr^{-1}
$M_{\rm H} = 0.15$–$0.4\ M_\odot$	$M_{\rm H} = 0.35\, M_\odot$	$M_{\rm H} = 0.39\, M_\odot$
$M_{\rm He} = 2.8$–$6.0\ M_\odot$	$M_{\rm He} = 4.81\, M_\odot$	$M_{\rm He} = 5.01\, M_\odot$

Note.
[a] The observational data of the progenitor SN 1993J are taken from Maund et al. (2004) and Sravan et al. (2020).

3.1.2. The Effect of Convective Overshoot

A larger convective overshoot parameter can cause the star to evolve redward further in the HR diagram. The reason is that the overshooting can lead to a larger convective core and extend the main sequence to lower effective temperature and

higher luminosity. Therefore, these effects can also give rise to a larger mass loss via stellar winds and a thinner hydrogen envelope after the ZAMS in Figure 1(b). For instance, at the end of the core hydrogen-burning phase, the stellar mass of model B1 with $\alpha_{\rm over} = 0.12$ is $16.46\,M_{\odot}$, whereas it is $16.07\,M_{\odot}$ for the model B3 with $\alpha_{\rm over} = 0.35$. Note that the overshoot parameter of 0.35 H_p is similar to that which Brott et al. (2011) deduced (i.e., $\alpha_{\rm over} = 0.335$).

This implies that mass loss at this age is closely related to the increased luminosity due to convective overshoot but, to a lesser extent, also on the effective temperature. However, the evolutionary track of the star computed with overshooting is much more extended toward lower effective temperatures at core hydrogen exhaustion. This implies a higher mass loss in model B3 and thus its mass is lower than the one of model B1 (see Table 2).

The hydrogen envelope decreases rapidly for a star with a larger overshoot parameter at core hydrogen exhaustion. Actually, the mass loss via stellar winds strongly depends on the stellar luminosity when the effective temperature decreases below 22,500 K (Vink et al. 2001). For example, the envelope mass for model B3 with $\alpha_{\rm over} = 0.35$ is $10.66\,M_{\odot}$, whereas it is $12.15\,M_{\odot}$ with $\alpha_{\rm over} = 0.12$. A larger core leads the star to evolve more rapidly to the red part of the HR diagram after the main-sequence phase. This means that a larger fraction of the core helium-burning phase occurs during the RSG phase where strong mass loss occurs. These strong mass losses favor a more rapid appearance of deep layers at the surface. During the first episode of RLOF, the hydrogen envelope of $11.08\,M_{\odot}$ in model B1 is transferred to the companion star while the hydrogen envelope of $9.36\,M_{\odot}$ is transferred to the companion star in B3. This implies that the more mass the hydrogen envelope retains during the main sequence, the more matter can be removed by RLOF.

Figure 2(b) shows the surface mass fraction ratio of nitrogen to carbon for a primary star with different overshoot parameters in a binary system as a function of the actual mass. The surface ratio of $^{14}N/^{12}C$ in the binary system B1 can attain a higher value of 93.370 compared to the value of 2.305 in its single-star counterpart S4 at core helium exhaustion (see Table 3). This is mainly because the surface chemical composition can be changed by the mass removal via RLOF. After the first RLOF event, the ratio of $^{14}N/^{12}C$ can attain a larger value of 112 in model B3 with a larger overshoot parameter. This is because the hydrogen-burning shell is located above the larger helium core and thus is buried in a shallow position of the hydrogen envelope. The envelope can develop a smaller outer convective region in this model. Therefore, the duration of the hydrogen-burning shell is very short because the hydrogen-burning shell can be easily exposed by RLOF. The results also show that severe stripping of the hydrogen envelope usually can give rise to a higher surface effective temperature.

3.1.3. The Effect of Metallicity

It is shown in Figure 1(c) that a decrease metallicity can trigger smaller mass loss via stellar winds and produce less-stripped progenitors of Type IIb SNe. The mass loss via stellar winds scales as $\dot{M}_{\rm wind} \propto Z^{0.85}$ (Vink et al. 2000; Vink & Sander 2021). Therefore, the total mass lost during the lifetime of the star is strongly correlated with the amount of metals present in the envelope. The star with low metallicity evolves essentially at almost constant mass during most of the main-sequence phase because of the absence of the larger mass loss via stellar winds. For this reason, the star with a lower metallicity has a thicker hydrogen envelope in comparison with its counterpart with higher metallicity. For example, when the core hydrogen is exhausted, the mass of the hydrogen envelope of model B4 with $Z = 0.008$ is $13.09\,M_{\odot}$, whereas it is $12.17\,M_{\odot}$ for model B5 with $Z = 0.03$. During the first episode of RLOF, $11.43\,M_{\odot}$ in model B4 with $Z = 0.008$ is transferred to the companion star, while it is $9.81\,M_{\odot}$ in the B3 with $Z = 0.03$. Therefore, we can infer that more mass can be transferred via RLOF for stars with the same mass by lower metallicity.

Figure 2(c) shows the surface mass fraction ratio of nitrogen to carbon for a primary star with different metallicities and rotational velocity as a function of the actual mass. The surface nitrogen $\log^{14}N$ has the same value of -3.394 as the initial one in the model B4 with $Z = 0.008$, while it is -2.996 in model B1 with $Z = 0.02$ before the onset of RLOF (see Table 3). At lower Z, there are less CNO elements, and thus the nitrogen abundance is in any case less (even the one resulting from the CNO process). This implies that the surface nitrogen cannot be suddenly enhanced by the first dredge-up and the bottom of the outer convection region does not touch the hydrogen-burning shell. It is shown that surface ^{14}N in the binary system B4 with a lower metallicity can attain a higher value after RLOF compared to its counterpart B5 with higher metallicity. The reason is that the total amount of mass transfer via RLOF is higher in the binary system with low metallicity.

The abundance of nitrogen is proportional to the initial metallicity prior to the core helium burning. The reaction of nitrogen via $^{14}N(\alpha, \gamma)^{18}F(e^{+}\ \nu)\ ^{18}O$ is an important exoergic process during the central helium-burning phase. Low metallicity has an important impact on the energy generation during hydrogen shell burning via the CNO cycle, which also affects the boundary condition for the helium core.

3.1.4. The Effect of Orbital Period

In Figure 1(d), it can be seen that RLOF is very efficient at removing the mass of the hydrogen envelope in contrast to stellar winds. Beyond core hydrogen exhaustion, the mass loss via stellar winds is $4.3\,M_{\odot}$ for the single star S4, whereas it is $11.08\,M_{\odot}$ during the first episode of mass transfer in model B1. This indicates that mass loss via stellar winds in the less massive star (i.e., $M < 19\,M_{\odot}$) is too weak to remove the thick hydrogen envelope and produces Type IIb SNe. The single star will explode as a Type IIP SN (see Table 1).

The transferred mass of the hydrogen envelope is very sensitive to the initial orbital period of the binary system. We note that an initially tighter orbit can result in a deeper stripping of the hydrogen envelope via RLOF. For example, the transferred matter is $9.23\,M_{\odot}$ for model B6 with $P_{\rm orb} = 3.0$ days whereas it is $6.34\,M_{\odot}$ for model B9 with $P_{\rm orb} = 1600.0$ days. The B6 system with $P_{\rm orb} = 3.0$ days undergoes strong Case A mass transfer, followed by a later episode of Case B mass transfer, with the last bit of remaining hydrogen removed by strong WR winds during the later core-burning phases. This model can produce a low-mass helium core with $M = 3.3\,M_{\odot}$ at the time of explosion, with a radius of about $4.26\,R_{\odot}$. However, the model B6 cannot be consistent with the observed hydrogen envelope mass of 0.03–0.5 $M_{\odot}$ for Type IIb because it completely loses any hydrogen envelope, even a thin one. It is also possible to produce fully stripped Type Ib progenitors

Table 3
Major Evolutionary Parameters for Nine Models Including Single Stars and the Primary Star in Binaries

Sequence	Age (Myr)	M_1 ($M_\odot$)	$\log\left(\frac{R}{R_\odot}\right)$	$\log T_{\rm eff}$ (K)	$\log\left(\frac{L}{L_\odot}\right)$	$\log T_{\rm c}$ (K)	$\log \rho_{c_3}$ (g cm^{-3})	$\frac{\rm N}{\rm N_{ini}}$	$V_{\rm eq}$ (km s^{-1})	$X_{\rm H}$	$Y_{\rm He}$	log(^{12}C)	log(^{14}N)	log(^{16}O)	$\frac{^{14}\rm N}{^{12}\rm C}$
ZAMS															
S1	0.103	15.000	0.694	4.487	4.290	7.534	0.787	0.995	0.000	0.700	0.280	−2.463	−2.996	−2.029	0.293
S4	0.144	17.000	0.726	4.510	4.447	7.543	0.734	0.993	0.000	0.700	0.280	−2.463	−2.996	−2.029	0.293
S6	0.169	17.000	0.768	4.483	4.422	7.541	0.741	1.000	400.00	0.700	0.280	−2.463	−2.996	−2.029	0.293
B1	0.104	16.999	0.725	4.511	4.446	7.543	0.737	1.000	0.000	0.700	0.280	−2.463	−2.996	−2.029	0.293
B3	0.174	16.998	0.726	4.510	4.448	7.543	0.734	1.000	0.000	0.700	0.280	−2.463	−2.996	−2.029	0.293
B4	0.043	17.000	0.698	4.512	4.397	7.560	0.811	1.000	0.000	0.736	0.256	−2.861	−3.394	−2.427	0.293
B6	0.107	16.999	0.725	4.511	4.446	7.543	0.737	1.000	0.000	0.700	0.280	−2.463	−2.996	−2.029	0.293
B9	0.104	16.999	0.725	4.511	4.446	7.543	0.737	1.000	0.000	0.700	0.280	−2.463	−2.996	−2.029	0.293
B11	0.199	16.997	0.769	4.483	4.423	7.540	0.740	1.000	400.00	0.700	0.280	−2.463	−2.996	−2.029	0.293
ECHB															
S1	11.642	14.619	1.075	4.391	4.670	7.732	1.301	1.000	0.000	0.700	0.280	−2.463	−2.996	−2.029	0.293
S4	9.900	16.506	1.124	4.405	4.820	7.743	1.257	1.000	0.000	0.700	0.280	−2.463	−2.996	−2.029	0.293
S6	12.841	15.993	1.105	4.445	4.943	7.751	1.224	8.488	131.725	0.596	0.384	−3.224	−2.068	−2.344	14.328
B1	9.923	16.455	1.119	4.406	4.816	7.744	1.265	1.000	0.000	0.700	0.280	−2.463	−2.996	−2.029	0.293
B3	11.136	16.069	1.315	4.332	4.913	7.759	1.271	1.000	0.000	0.700	0.280	−2.463	−2.996	−2.029	0.293
B4	11.133	16.797	1.075	4.424	4.800	7.864	1.776	1.000	0.000	0.736	0.256	−2.861	−3.394	−2.427	0.293
B6	10.629	7.479	1.148	4.307	4.478	7.746	1.457	5.712	0.000	0.691	0.288	−4.487	−2.240	−2.072	176.912
B9	9.923	16.455	1.119	4.406	4.816	7.744	1.265	1.000	0.000	0.700	0.280	−2.463	−2.996	−2.029	0.293
B11	11.808	15.774	1.158	4.402	4.877	7.746	1.238	6.529	72.147	0.654	0.326	−3.037	−2.182	−2.197	7.167
BCHEB															
S1	11.642	14.619	1.075	4.391	4.670	7.732	1.301	1.000	0.000	0.700	0.280	−2.463	−2.996	−2.029	0.293
S4	9.905	16.504	1.102	4.422	4.845	7.816	1.525	1.000	0.000	0.700	0.280	−2.463	−2.996	−2.029	0.293
S6	12.846	15.993	1.075	4.467	4.971	7.839	1.534	8.488	144.644	0.596	0.384	−3.224	−2.068	−2.344	14.331
B1	9.941	16.449	1.385	4.286	4.866	8.038	2.548	1.000	0.000	0.700	0.280	−2.463	−2.996	−2.029	0.293
B3	11.148	16.061	1.586	4.202	4.934	8.054	2.384	1.000	0.000	0.700	0.280	−2.463	−2.996	−2.029	0.293
B4	11.145	16.795	1.329	4.302	4.820	8.053	2.633	1.000	0.000	0.736	0.256	−2.861	−3.394	−2.427	0.293
B6	10.659	5.554	1.392	4.240	4.696	8.042	2.902	12.422	0.000	0.300	0.681	−4.037	−1.902	−3.176	136.285
B9	9.941	16.449	1.385	4.285	4.866	8.038	2.549	1.000	0.000	0.700	0.280	−2.463	−2.996	−2.029	0.293
B11	11.827	15.763	1.663	4.159	4.917	8.063	2.536	6.530	31.258	0.654	0.326	−3.037	−2.182	−2.197	7.171
ECHEB															
S1	12.788	12.926	2.881	3.541	4.878	8.905	5.430	3.943	0.000	0.645	0.334	−2.699	−2.401	−2.103	1.987
S4	10.988	13.447	2.880	3.548	4.907	8.478	3.587	4.334	0.000	0.632	0.348	−2.722	−2.360	−2.120	2.305
S6	13.761	9.950	2.956	3.582	5.192	8.911	5.297	10.065	0.077	0.467	0.513	−3.544	−1.994	−2.505	35.495
B1	10.924	5.177	2.687	3.665	4.987	8.906	5.307	9.619	0.000	0.478	0.502	−3.984	−2.013	−2.411	93.370
B3	11.918	5.442	0.194	4.943	5.113	8.922	5.232	12.493	0.000	0.000	0.981	−3.567	−1.900	−3.461	46.424
B4	12.153	5.011	2.712	3.639	4.933	8.902	5.343	9.985	0.000	0.526	0.466	−4.351	−2.395	−2.860	90.439
B6	12.000	3.347	0.626	4.627	4.715	8.885	5.486	12.546	0.000	0.000	0.981	−3.626	−1.898	−3.480	53.502
B9	10.909	6.848	2.955	3.533	4.993	8.905	5.318	5.874	0.000	0.584	0.396	−2.851	−2.228	−2.190	4.207
B11	12.668	5.202	0.234	4.913	5.074	8.918	5.257	12.353	95.589	0.000	0.975	−2.289	−1.905	−3.257	2.424
BCCB															
S1	12.788	12.926	2.881	3.541	4.878	8.905	5.430	3.943	0.000	0.645	0.334	−2.699	−2.401	−2.103	1.987
S4	11.013	13.327	2.982	3.532	5.046	8.807	5.148	4.978	0.000	0.615	0.365	−2.780	−2.299	−2.146	3.023
S6	13.761	9.950	2.956	3.582	5.192	8.911	5.297	10.065	0.077	0.467	0.513	−3.544	−1.994	−2.505	35.495

Table 3
(Continued)

Sequence	Age (Myr)	M_1 ($M_\odot$)	$\log\left(\frac{R}{R_\odot}\right)$	$\log T_{\rm eff}$ (K)	$\log\left(\frac{L}{L_\odot}\right)$	$\log T_{\rm c}$ (K)	$\log \rho_{\rm c}$ (g cm^{-3})	$\frac{\rm N}{\rm N_{ini}}$	$V_{\rm eq}$ (km s^{-1})	$X_{\rm H}$	$Y_{\rm He}$	log(^{12}C)	log(^{14}N)	log(^{16}O)	$\frac{^{14}\rm N}{^{12}\rm C}$
B1	10.924	5.177	2.687	3.665	4.987	8.906	5.307	9.619	0.000	0.478	0.502	−3.984	−2.013	−2.411	93.370
B3	11.918	5.442	0.194	4.943	5.113	8.922	5.232	12.493	0.000	0.000	0.981	−3.567	−1.900	−3.461	46.424
B4	12.153	5.011	2.712	3.639	4.933	8.902	5.343	9.985	0.000	0.526	0.466	−4.351	−2.395	−2.860	90.439
B6	12.000	3.347	0.626	4.627	4.715	8.885	5.486	12.546	0.000	0.000	0.981	−3.626	−1.898	−3.480	53.502
B9	10.909	6.848	2.955	3.533	4.993	8.905	5.318	5.874	0.000	0.584	0.396	−2.851	−2.228	−2.190	4.207
B11	12.668	5.202	0.234	4.913	5.074	8.918	5.257	12.353	95.589	0.000	0.975	−2.289	−1.905	−3.257	2.424
ECCB															
S1	12.789	12.922	2.885	3.540	4.884	8.933	5.941	3.977	0.000	0.644	0.336	−2.701	−2.397	−2.104	2.015
S4	11.015	13.316	2.976	3.533	5.038	8.944	5.974	4.991	0.000	0.614	0.366	−2.781	−2.298	−2.146	3.039
S6	13.761	9.947	2.953	3.581	5.182	8.949	5.851	10.083	0.082	0.465	0.516	−3.546	−1.993	−2.508	35.715
B1	10.925	5.169	2.688	3.667	4.997	8.938	5.850	9.630	0.000	0.477	0.503	−3.983	−2.013	−2.413	93.333
B3	11.919	5.441	0.224	4.930	5.119	8.917	5.749	12.493	0.000	0.000	0.981	−3.567	−1.900	−3.461	46.424
B4	12.154	5.002	2.713	3.641	4.944	8.938	5.866	10.013	0.000	0.525	0.467	−4.350	−2.394	−2.864	90.444
B6	12.003	3.341	0.720	4.581	4.717	8.928	6.012	12.546	0.000	0.000	0.981	−3.625	−1.898	−3.481	53.334
B9	10.910	6.833	2.956	3.535	5.006	8.937	5.846	5.899	0.000	0.583	0.397	−2.854	−2.226	−2.191	4.250
B11	12.669	5.200	0.268	4.898	5.081	8.923	5.760	12.348	83.027	0.000	0.975	−2.287	−1.905	−3.256	2.408
BCNEB															
S1	12.790	12.919	2.875	3.542	4.870	9.178	7.165	3.984	0.000	0.644	0.336	−2.701	−2.396	−2.105	2.020
S4	11.015	13.316	2.977	3.533	5.038	9.181	6.849	4.991	0.000	0.614	0.366	−2.781	−2.298	−2.146	3.039
S6	13.761	9.946	2.951	3.583	5.187	9.178	6.852	10.093	0.083	0.463	0.517	−3.547	−1.992	−2.509	35.827
B1	10.925	5.165	2.682	3.664	4.974	9.179	7.071	9.636	0.000	0.477	0.503	−3.982	−2.013	−2.413	93.301
B3	11.919	5.440	0.245	4.917	5.113	9.180	6.679	12.493	0.000	0.000	0.981	−3.567	−1.900	−3.461	46.424
B4	12.155	4.998	2.711	3.639	4.931	9.182	7.128	10.032	0.000	0.525	0.467	−4.349	−2.393	−2.867	90.437
B6	…	…	…	…	…	…	…	…	…	…	…	…	…	…	…
B9	10.910	6.825	2.954	3.534	4.996	9.180	7.048	5.915	0.000	0.583	0.397	−2.856	−2.225	−2.192	4.277
B11	12.669	5.199	0.303	4.878	5.071	9.125	6.804	12.346	71.602	0.000	0.975	−2.285	−1.905	−3.256	2.401
ECNEB															
S1	12.790	12.919	2.876	3.541	4.870	9.284	6.968	3.984	0.000	0.644	0.336	−2.701	−2.396	−2.105	2.020
S4	11.015	13.316	2.978	3.532	5.038	9.302	6.772	4.991	0.000	0.614	0.366	−2.781	−2.298	−2.146	3.039
S6	13.761	9.946	2.953	3.582	5.189	9.309	6.682	10.093	0.082	0.463	0.517	−3.547	−1.992	−2.509	35.827
B1	10.925	5.165	2.684	3.664	4.979	9.275	7.048	9.636	0.000	0.477	0.503	−3.982	−2.013	−2.413	93.301
B3	11.919	5.440	0.282	4.895	5.098	9.265	6.968	12.493	0.000	0.000	0.981	−3.567	−1.900	−3.461	46.424
B4	12.155	4.998	2.713	3.639	4.936	9.262	6.924	10.032	0.000	0.525	0.467	−4.349	−2.393	−2.867	90.437
B6	…	…	…	…	…	…	…	…	…	…	…	…	…	…	…
B9	10.910	6.825	2.954	3.534	4.996	9.180	7.048	5.915	0.000	0.583	0.397	−2.856	−2.225	−2.192	4.277
B11	12.669	5.199	0.326	4.866	5.070	9.310	7.705	12.346	71.202	0.000	0.975	−2.285	−1.905	−3.256	2.401
BROLF1															
B1	9.955	16.442	2.368	3.789	4.843	8.195	2.928	1.000	0.000	0.700	0.280	−2.463	−2.996	−2.029	0.293
B3	11.152	16.058	2.371	3.794	4.869	8.168	2.761	1.000	0.000	0.700	0.280	−2.463	−2.996	−2.029	0.293
B4	11.164	16.789	2.363	3.775	4.778	8.218	3.024	1.000	0.000	0.736	0.256	−2.861	−3.394	−2.427	0.293
B6	8.534	16.835	1.037	4.424	4.724	7.585	0.768	1.000	0.000	0.700	0.280	−2.463	−2.996	−2.029	0.293
B9	9.966	16.423	2.840	3.531	4.757	8.211	2.961	2.176	0.000	0.685	0.294	−2.563	−2.659	−2.048	0.801
B11	11.832	15.760	2.378	3.783	4.843	8.164	2.857	6.530	5.519	0.654	0.326	−3.037	−2.182	−2.197	7.174

Table 3
(Continued)

Sequence	Age (Myr)	M_1 ($M_\odot$)	$\log\left(\frac{R}{R_\odot}\right)$	$\log T_{\rm eff}$ (K)	$\log\left(\frac{L}{L_\odot}\right)$	$\log T_{\rm c}$ (K)	$\log \rho_{\rm c}$ (g cm^{-3})	$\frac{\rm N}{\rm N_{ini}}$	$V_{\rm eq}$ (km s^{-1})	$X_{\rm H}$	$Y_{\rm He}$	log(^{12}C)	log(^{14}N)	log(^{16}O)	$\frac{^{14}\rm N}{^{12}\rm C}$
EROLF1															
B1	9.964	5.594	2.671	3.618	4.768	8.206	2.945	9.575	0.000	0.479	0.501	−3.915	−2.015	−2.408	79.428
B3	11.159	6.820	2.574	3.751	5.104	8.204	2.807	9.441	0.000	0.514	0.466	−3.766	−2.021	−2.398	55.484
B4	11.174	5.372	2.688	3.598	4.720	8.224	3.025	9.866	0.000	0.528	0.464	−4.294	−2.400	−2.846	78.234
B6	10.493	7.500	1.215	4.260	4.425	7.636	1.118	5.712	0.000	0.691	0.288	−4.487	−2.240	−2.072	176.911
B9	9.997	10.171	2.887	3.510	4.766	8.230	2.999	4.372	0.000	0.626	0.354	−2.714	−2.356	−2.126	2.280
B11	11.846	6.866	2.614	3.718	5.054	8.208	2.893	11.019	0.385	0.375	0.605	−3.609	−1.954	−2.683	45.107
BROLF2															
B1	10.916	5.241	2.665	3.664	4.940	8.706	4.682	9.589	0.000	0.479	0.502	−3.960	−2.015	−2.408	88.108
B3	…	…	…	…	…	…	…	…	…	…	…	…	…	…	…
B4	12.134	5.194	2.684	3.625	4.819	8.621	4.397	9.868	0.000	0.528	0.464	−4.295	−2.400	−2.846	78.485
B6	10.635	7.478	1.215	4.283	4.515	7.811	1.791	5.712	0.000	0.691	0.288	−4.487	−2.240	−2.072	176.912
B9	10.519	8.940	2.888	3.509	4.765	8.286	3.077	4.372	0.000	0.626	0.354	−2.714	−2.356	−2.126	2.280
B11	…	…	…	…	…	…	…	…	…	…	…	…	…	…	…
EROLF2															
B1	…	…	…	…	…	…	…	…	…	…	…	…	…	…	…
B3	…	…	…	…	…	…	…	…	…	…	…	…	…	…	…
B4	…	…	…	…	…	…	…	…	…	…	…	…	…	…	…
B6	10.680	3.976	1.553	4.167	4.727	8.179	3.126	12.543	0.000	0.169	0.811	−3.927	−1.898	−3.309	106.831
B9	…	…	…	…	…	…	…	…	…	…	…	…	…	…	…
B11	…	…	…	…	…	…	…	…	…	…	…	…	…	…	…
EOC															
S1	12.790	12.919	2.876	3.541	4.869	9.301	7.569	3.984	0.000	0.644	0.336	−2.701	−2.396	−2.105	2.020
S4	11.015	13.316	2.977	3.532	5.039	9.301	7.473	4.991	0.000	0.614	0.366	−2.781	−2.298	−2.146	3.039
S6	13.761	9.946	2.956	3.580	5.186	9.735	8.990	10.093	0.082	0.463	0.517	−3.547	−1.992	−2.509	35.827
B1	10.925	5.165	2.685	3.661	4.968	9.933	9.652	9.636	0.000	0.477	0.503	−3.982	−2.013	−2.413	93.301
B3	11.919	5.440	0.320	4.869	5.070	9.956	9.908	12.493	0.000	0.000	0.981	−3.567	−1.900	−3.461	46.424
B4	12.155	4.998	2.714	3.638	4.935	9.953	9.765	10.032	0.000	0.525	0.467	−4.349	−2.393	−2.867	90.437
B6	12.005	3.339	0.818	4.519	4.665	8.979	7.211	12.545	0.000	0.000	0.981	−3.624	−1.898	−3.481	53.243
B9	10.910	6.825	2.955	3.532	4.992	9.940	9.626	5.915	0.000	0.583	0.397	−2.856	−2.225	−2.192	4.277
B11	12.669	5.199	0.420	4.803	5.005	9.496	8.485	12.346	57.367	0.000	0.975	−2.285	−1.905	−3.256	2.401

Note. Abbreviations: ZAMS: zero-age main sequence; ECHB: the end of core hydrogen burning; ECHEB: the end of core helium burning; ECCB: the end of core carbon burning; BCNEB: the beginning of core neon burning; ECNEB: the end of core neon burning; BROLF1: the beginning of the first episode of RLOF; EROLF1: the end of the first episode of RLOF; BROLF2: the beginning of the second episode of RLOF; EROLF2: the end of the second episode of RLOF; BROLF3: the beginning of the third episode of RLOF; EROLF3: the end of the third episode of RLOF; EOC: the end of the calculation.

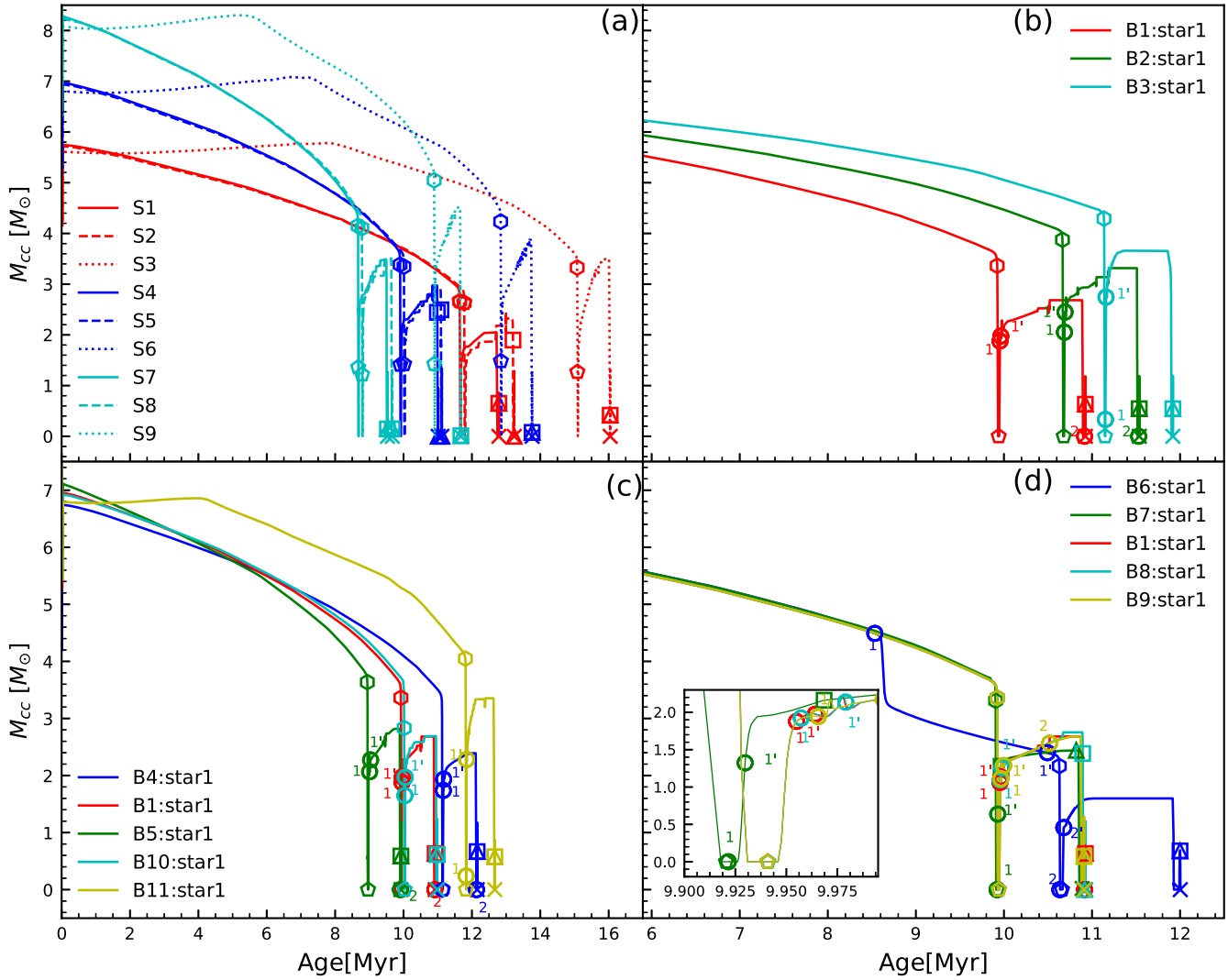

Figure 3. Convective cores as a function of evolutionary age. (a) For single stars with various initial masses and rotational velocities. (b) For primary stars with various overshoot parameters in a binary system with an initial $P_{\rm orb} = 300$ days. (c) For primary stars with various initial rotational velocities and metallicities in a binary system with an initial $P_{\rm orb} = 300$ days. (d) For primary stars in a binary system with various initial orbital periods.

(see Table 1 and Figure 6; Yoon et al. 2010; Yoon 2015). The model B9 finally explodes as a Type IIP SN because its hydrogen envelope remains sufficiently large to preserve the RSG structure. These facts imply that the relationship of SN IIb with other types of SNe, such as SNe IIP, IIL, and Ib/c, is closely bound up to the hydrogen envelope mass. Moreover, various types of SNe IIb are also related to the hydrogen envelope mass.

A system with a region 300 days $< P_{\rm orb} <$ 700 days can give rise to an RSG-type SN IIb progenitor. The initial period of 300 days roughly separates between RSG-type SN IIb progenitors and YSG-type SN IIb progenitors. The binary system B7, with an initial $P_{\rm orb} = 30$ days, can produce a BSG-type SN IIb progenitor (see Figure 6). Thus, binary models with orbital periods ranging from $\sim$10 days $< P_{\rm orb} <$ 700 days may turn into SNe IIb (see Figure 5(d)). Most importantly, the amount of mass transfer via RLOF is closely related not only to the initial orbital period but also to the thickness of the hydrogen or helium envelopes. Beyond core hydrogen exhaustion, a larger amount of the residual hydrogen in the envelope can expand to a larger radius during the late evolutionary stages in contrast to a bare helium core. After the core helium-burning phase, the envelope expansion becomes more significant for more compact stellar cores.

Figure 2(d) shows the surface mass fraction ratio of nitrogen to carbon as a function of the orbital period for a primary star in a binary system with different initial orbital periods. One can see that the donor star in binaries can experience envelope peeling, which can expose the inner layers of CNO-processed material to the surface, increasing the surface abundance of nitrogen. An initial tighter orbit results in more significant peeling of the hydrogen envelope, and vice versa. The system with the shortest orbital period has the highest surface N/C ratio in our grid. The main reason is that the hydrogen-burning shell can be revealed early because much more of a hydrogen envelope can be eliminated by RLOF.

3.2. The Evolution of the Convective Core and Helium Core

3.2.1. The Effect of Rotation

Figure 3(a) shows the convective cores of nonrotating and rotating single stars as a function of evolutionary age. The mass of the convective core increases with the initial mass of the star because the size of the convective core is governed by radiative

pressure, which is proportional to the quadrature of core temperature T^4. Actually, at the onset of evolution, the centrifugal force partially sustains the gravity but most of the equilibrium is due to the pressure gradient. Therefore, the rotating star behaves like a less massive nonrotating one, and the mass of the convective core is smaller. This results in a lower luminosity in the HR diagram. The rotating star has a slightly denser and cooler core than the nonrotating one.

As the evolution proceeds, the rotation-induced mixing starts to refuel the core with fresh hydrogen. The mass of the convective core is larger in models with higher initial rotational velocity because the rotation-induced mixing becomes very efficient at rapidly rotating stars. Actually, two main physical processes are responsible for such a rotational mixing: meridional circulation and secular shear. Meridional circulations, which are scaled as the square of rotational angular velocity, are mainly responsible for rotational mixing above the convective core (Maeder & Meynet 2000a; Song et al. 2018). Rotational mixing can slow down the decrease in mass of the convective core and is similar to the behavior of overshooting. The larger core induced by rotational mixing leads to a higher central temperature and a lower opacity in the outer envelope. Rotating stars have larger convective cores than nonrotating ones.

Figure 4 displays the mass of the helium core as a function of evolutionary age. The mass of the helium core generally scales with the size of the hydrogen convective core and increases with increasing initial rotational velocities and stellar masses (see Figure 4(a)). Generally, the larger the size of the convective core, the larger the final helium core mass would be at the end of the main sequence. The maximum size of the hydrogen convective core generally increases with the mass of the star and the rotational velocities. Therefore, the helium core at core helium exhaustion can increase with the mass of the star and rotational velocities, as well. Furthermore, the main consequence of the rotational mixing is the increase of the lifetime of the core hydrogen burning. The main reason is that fresh hydrogen in the outer envelope is transferred into the central core by rotational mixing. This mixing process increases the hydrogen fuel supply in the stellar core.

The wind mass-loss rate of single stars with $M \geqslant 30\,M_{\odot}$ is strong enough to remove the hydrogen envelope, and these stars are expected to generate Type IIb SNe (Heger et al. 2003; Georgy et al. 2009). This type of star has a helium core mass $\geqslant 8\ M_{\odot}$ previous to the explosion. However, a $8\,M_{\odot}$ helium core is too massive to produce the second maximum at ∼20 days as observed in the light curves for SN 2011dh, even assuming the most extreme ^{56}Ni mixing (Bersten et al. 2012). The helium core mass of single stars goes up because of the creation of helium by the hydrogen-burning shell (see Figure 4(a)). However, one can see that the mass of the helium core in model B6 can be greatly influenced by the RLOF during the main sequence (see Figure 4(d)). This is because the convective core can be greatly reduced by the RLOF. This fact indicates that, for a given initial mass, a star in a binary system has a smaller core mass than its single counterpart. However, the corresponding radii go up with a decrease of the core helium mass (Yoon et al. 2010, 2017). After the main sequence, the evolution of the helium core is almost unaffected by the mass transfer. The helium produced by the hydrogen-burning shell contributes little to the mass of the core helium. The binary-peeled star loses matter after the RLOF because of strong stellar winds, leading to a reduction in the helium core mass. Therefore, the amount of oxygen that can be produced from a specific exploding core is smaller in an initially tighter system.

However, the mass fraction of the convective core in slowly rotating massive stars with $v_{\rm ini} = 200$ km s^{-1} is slightly smaller than the nonrotating stars beyond core hydrogen exhaustion. Rotational mixing plays a minor role in this case. During the core helium-burning phase, the convective core grows largely because the mass of the helium core itself grows regardless of the strong mass losses via the stellar winds. As the mass of the core grows, its luminosity increases accordingly but the radius of the convective core remains constant. Therefore, the mass-loss rate of stellar winds can grow rapidly. Meanwhile, the central temperature and density go up accordingly. This favors the formation of convection. The helium-burning convective core grows until close to the time of core helium exhaustion because the central temperature increases due to the decrease of the fuel supply. This actually increases the energy generation rate and thus the convective core. This growth of the helium core can have a very important consequence. The addition of helium to the helium convection zone at a late time increases the O/C ratio made by helium burning.

3.2.2. The Effect of Convective Overshoot

Overshooting can cause the convective core to grow in mass, and this leads to the mixing of fresh hydrogen above the core into the central nuclear-burning zone. Therefore, overshooting has the effect of extending the main-sequence lifetime. The band of the main sequence extends to lower effective temperature values when convective core overshoot is larger. A massive star with initial $M > 19\,M_{\odot}$ has a helium core $M_{\rm He} > 6\,M_{\odot}$ prior to the SN explosion (see Figure 4(a)). This fact indicates that a low-mass progenitor of a SNe Ib can only be produced in the maximum mass limit $\sim 19\ M_{\odot}$.

The amount of helium in the envelope can also be convected into the helium core near central helium exhaustion by convective overshoot. At the stage of advanced nuclear burning, a higher overshoot parameter leads to slightly higher helium and carbon core masses (see Figure 4(c)). However, the lifetime during helium burning might be reduced by convective overshoot because the central temperature can be increased. The efficiency of helium combustion becomes higher because of the enlarged helium core. For example, the lifetime of the core helium burning in model B1 with $\alpha_{\rm over} = 0.12$ is about 0.97 Myr, whereas it is about 0.76 Myr in model B3 with $\alpha_{\rm over} = 0.35$ (see Table 3).

3.2.3. The Effect of Metallicity

The effect of metallicity on the convective core mass is illustrated in Figure 3(c). At the beginning of the evolution, the convective core decreases with decreasing metallicity. The reason is that a lower initial metallicity also indicates a reduction of the abundance of the CNO nuclei and therefore a decrease of the hydrogen-burning efficiency. It has been shown in the second half of the main sequence that this situation can change under different conditions. In order to maintain higher luminosity, the star has to contract more to increase the core temperature and the nuclear energy production. The convective core can be enlarged by the increased central temperature. Moreover, the initial metallicity has an important impact on

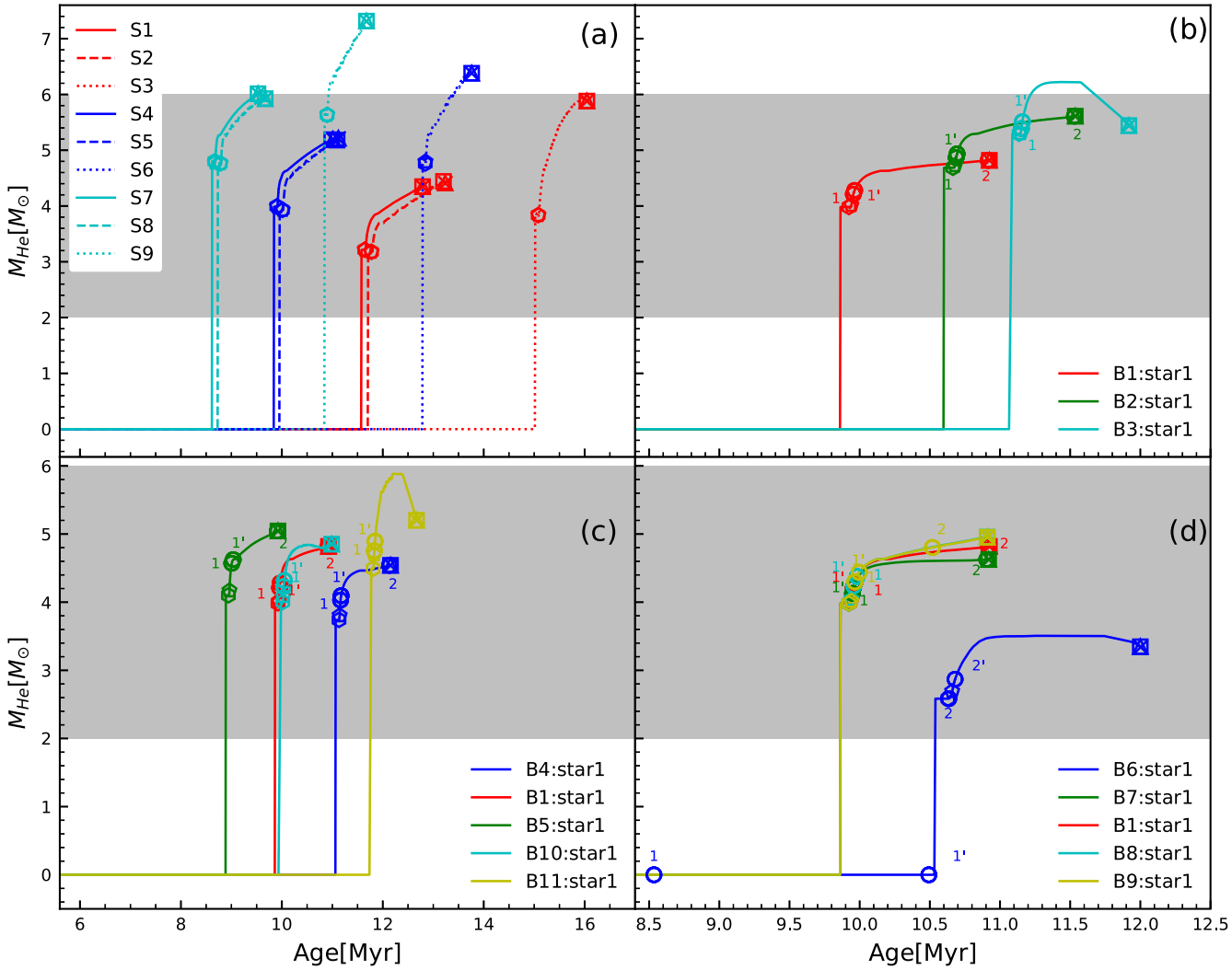

Figure 4. The mass of the helium core as a function of evolutionary age. (a) For single stars with different initial masses and rotational velocities. (b) For primary stars with different overshoot parameters in a binary system with an initial $P_{\rm orb} = 300$ days. (c) For primary stars with different initial metallicities and rotational velocities in a binary system with an initial $P_{\rm orb} = 300$ days. (d) For primary stars in a binary system with different initial orbital periods. Observations for helium core masses of SNe IIb, which are indicated in shaded regions, are 2–6.0 $M_\odot$.

initial hydrogen and helium abundances. For lower metallicity, there is more hydrogen to burn in the central core. The lifetime of the main sequence can be enlarged by the fresh fuel supply.

The effect of metallicity on the helium core mass is shown in Figure 4(c). Limongi & Chieffi (2018) demonstrated that less massive stars (i.e., $<40\,M_\odot$) develop helium core masses essentially independent of the initial metallicity in single stars. This implies that the mass of the helium convective core weakly depends on the metallicity. However, we can see that a smaller mass helium convective core (or helium core) can come into being in a low-metallicity environment after core hydrogen depletion (see Figure 3(c)). Moreover, in massive stars with low metallicity, the helium convective core can grow to such an extent during central helium burning that it approaches the hydrogen-burning shell. Furthermore, the helium convective core never recedes until core helium exhaustion. The reason is that the conversion of helium to carbon and oxygen increases the opacity in the entire convective core so that its outer border is continuously pushed outward rather than inward. Hence, a strong chemical discontinuity forms at the border of the helium convective core where the helium abundance changes from roughly zero to roughly one at central helium exhaustion. A helium convective shell starts to form outside the maximum extension of the convective core whereas the chemical composition of this region is still the one left by hydrogen burning.

3.2.4. The Effect of the Orbital Period

From Figure 3(d), one can also notice that the mass of the convective core drops from 4.44 $M_\odot$ to 2.73 $M_\odot$ during the first episode of RLOF for model B6 with initial $P_{\rm orb} = 3.0$ days. The result shows that a primary star which loses its hydrogen envelope via RLOF will develop a smaller convective core than its single counterpart. This fact indicates that RLOF can accelerate the mass decrease of the convective core during the main-sequence phase. The reason is that the core temperature can be reduced significantly by RLOF. However, mass transfer via RLOF has the effect of extending the main-sequence lifetime of the primary star because the efficiency of hydrogen burning via the CNO cycle is extremely sensitive to the core temperature. The convective core after main sequence is also influenced by the previous RLOF because it displays a smaller

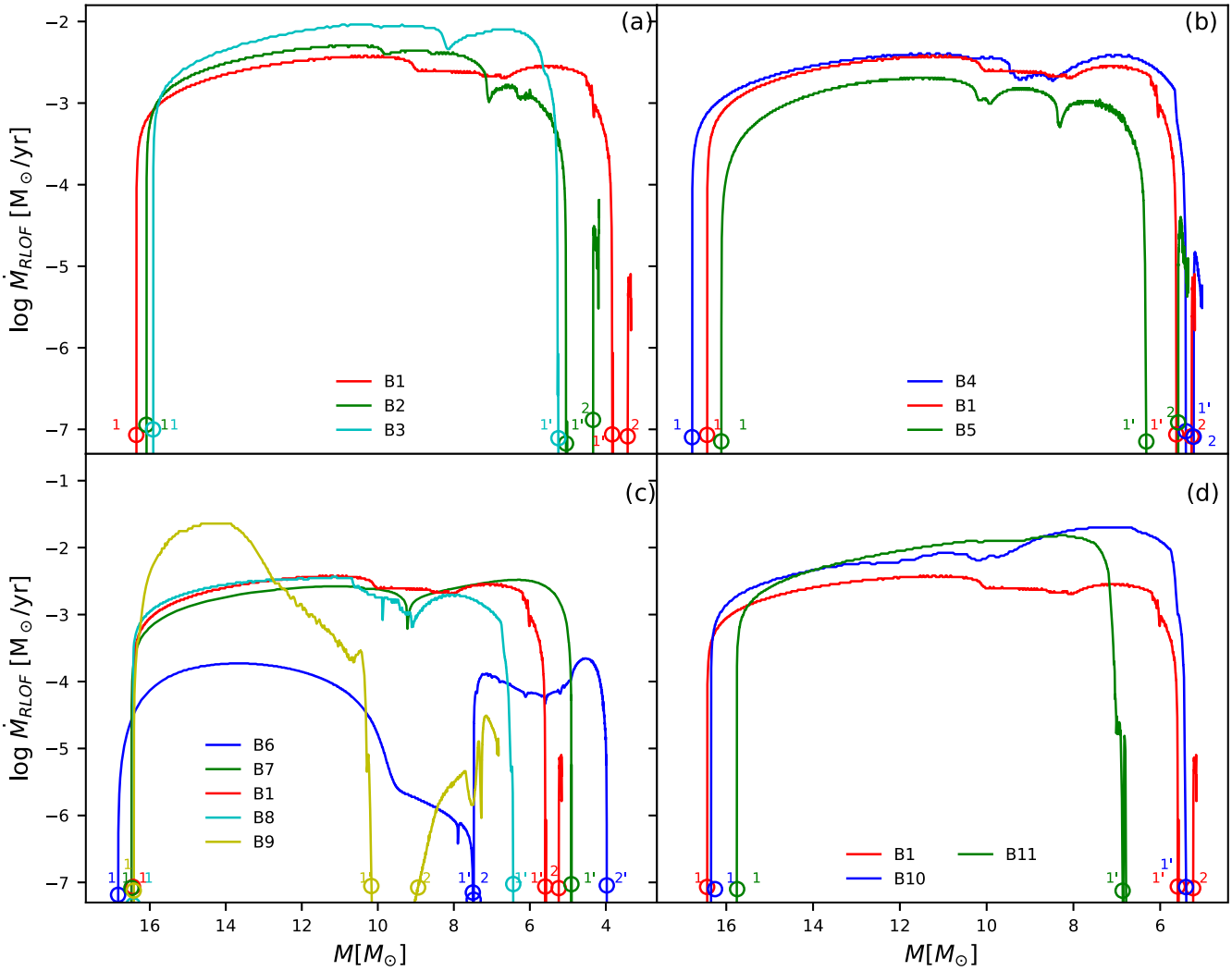

Figure 5. The rate of mass transfer via RLOF as a function of evolutionary age. (a) For primary stars with various overshoot parameters in a binary system with an initial $P_{\rm orb} = 300$ days. (b) For primary stars with various initial metallicities in a binary system with an initial $P_{\rm orb} = 300$ days. (c) For primary stars in a binary system with various initial orbital periods. (d) For primary stars with various initial rotational velocities in a binary system with an initial $P_{\rm orb} = 300$ days.

value after main sequence than the counterpart with initial $P_{\rm orb} = 300$ days in model B1.

The effect of the orbital period on the helium core mass is shown in Figure 4(c). The helium core formed in binary systems is less massive than the single counterpart by comparing model S4 with B6. This can be explained by an early onset of Case A mass transfer in this system and a significant loss of matter during this process. Case A mass transfer takes place in the primary star of model B6 before the helium core is fully formed. The mass loss via RLOF is strong enough to decrease substantially the total mass and therefore to induce a reduction of the convective core during the main sequence. The primary star in this system loses about 12.8 $M_\odot$ during all binary interactions via RLOF. As a consequence, in this case the helium core at core helium depletion is smaller than it would be in Case B or Case C mass transfer.

In actual fact, the evolution of the star after core hydrogen burning mainly depends on the mass of the helium core rather than the total mass. This property implies that mass loss via RLOF globally affects the evolution during the main sequence because it is efficient enough to determine the reduction of the mass of the hydrogen convective core, which in turn is mainly responsible for the initial mass of the helium core. A small convective core develops in an initially tighter binary system. RLOF in Case B or Case C has little impact on the evolution of the convective core (see Figure 4(d)). The growth of the mass of a helium core can be merely affected by the development of the hydrogen-burning shell. However, the shell can be removed or extinguished by RLOF, as shown in model B6 with an initial $P_{\rm orb} = 3.0$ days.

3.3. The Evolution of the Rate of Mass Transfer via Roche Lobe Overflow

3.3.1. The Effect of Convective Overshoot

When the primary star expands beyond its Roche lobe, mass is transferred to the companion. It is the expansion of the donor due to its own nuclear evolution that initiates mass transfer. Actually, the expansion of stellar radii makes the primary star continue to fill its Roche lobe and to trigger mass transfer via RLOF. From Figure 5(a), one can see that the maximum rate of mass transfer is closely related to convective overshooting. The maximum rate of the mass transfer via RLOF increases with the overshoot parameter. This can be understood by the fact that larger radii can be induced by the larger convective overshoot parameter and the mass-transfer rate has an exponential

dependence on stellar radius. The first maximum value of the mass-transfer rate heavily depends on the termination of decreasing of the orbital period at mass ratio one, $q = \frac{M_2}{M_1}$. When the primary star has a radiative envelope in Case A and early Case B mass transfer, the mass transfer via RLOF happens on the Kelvin–Helmholtz timescale. The primary shrinks rapidly in response to mass loss (i.e., the adiabatic mass–radius exponent $\zeta_{\rm ad} = \left(\frac{d\log R}{d\log M}\right)_{\rm ad} \gg 0$) while the Roche lobe contracts in response to mass loss, as well (see Figure 6(f)). RLOF can proceed only if the Roche lobe is slightly smaller than the stellar radius. One can find that the number of episodes of mass transfer via RLOF might decrease with increasing of the overshoot parameter. It is closely related not only to the residual amount of the hydrogen envelope but also to the orbital period of the system. Moreover, the expansion of the helium envelope beyond the core carbon exhaustion becomes more prominent for a more compact carbon–oxygen (CO) core via the mirror effect.

In fact, the final orbital period of the binary system goes up with the total amount of mass transfer via RLOF. The RLOF ceases when the donor loses most (but not all) of its hydrogen-rich layers. The primary star still has some hydrogen left in its envelope (typically a few 0.1 $M_\odot$). Moreover, the mass transfer occurs early in the star with a smaller convective parameter. For example, the model B1 with $\alpha_{\rm over} = 0.12$ undergoes RLOF at 9.95 Myr whereas the model B3 with $\alpha_{\rm over} = 0.35$ undergoes RLOF at 11.15 Myr. The main reason is that the lifetime has been enlarged by the convective overshooting parameter. The model with higher overshooting is redder and more extended than the one with smaller overshooting, and therefore is more prone to go through a stronger mass-transfer episode during the RSG phase.

Mass-transfer rates via RLOF can be very high (i.e., 10^{-2}–$10^{-3}\,M_\odot$ yr^{-1}), and can far exceed any mass-loss rate for a line-driven wind. The binary evolutionary channel supports the formation of Type IIb SNe. The observation of the binary companion in the case of the Type IIb SN 1993J, and possibly also in the case of SN 2013df, implies the binary channel. Although RLOF is the main physical process for mass removal, it cannot completely eliminate the whole hydrogen envelope from the primary star. Whether the SN progenitor can retain a large amount of hydrogen is closely related to the subsequent mass loss via stellar winds. Stellar winds are stronger in conditions of larger overshooting and favor the formation of SN IIb (see Figure 7(b)).

3.3.2. The Effect of Metallicity

From Figure 5(b), one can see that the maximum rate of mass transfer via RLOF also depends heavily on the metallicity. The smaller the metallicity, the greater the maximum mass-transfer rates. In fact, stellar winds for two components of the binary system tend to widen the binary separation and reduce the total amount of mass lost by RLOF. Stars with low metallicity have weaker stellar winds and more mass of hydrogen envelopes available for mass transfer via RLOF. Thus, the sizes of the Roche lobes become smaller in systems with low metallicities. More hydrogen can be retained before the onset of RLOF in the model with the lower metallicity. Therefore, less hydrogen is retained after the RLOF phase in the lower metallicity model (see Figure 1(c)). The mass-transfer rate depends very sensitively on the fractional radius excess of the donor, $\frac{\triangle R}{R_L} = \frac{R_D - R_L}{R_L}$. R_D is the radius of the donor while $R_{\rm L}$ is the radius of the Roche lobe. The quantity $\triangle R$ is the radius excess. This implies that the quantity $\triangle R$ is larger for stars with lower metallicity. One can also notice that the higher the metallicity, the earlier RLOF begins. For example, model B5 with $Z = 0.03$ commences RLOF at the age of 9.0 Myr, whereas model B4 with $Z = 0.008$ commences RLOF at the age of 11.16 Myr. The main reason is that stars with higher metallicity have larger stellar radii.

It can be noticed that stars with low metallicity are prone to generate more compact blue progenitors and retain less hydrogen mass at the end of RLOF in contrast to the counterparts high metallicity. However, the stellar winds after RLOF are stronger for stars with high metallicity. It favors a higher effective temperature because the thin hydrogen envelope can be removed.

3.3.3. The Effect of Orbital Period

From Figure 5(c), one can see that the maximum rate of mass transfer via RLOF also depends heavily on the orbital period. One can notice that the mass-transfer rate is larger for an initially wider binary system because the primary star is farther evolved. Mass transfer becomes increasingly unstable and rapid from Case A mass transfer to Case C mass transfer. Case A mass transfer occurs in system B6 with the shortest initial orbit period. The first phase of mass transfer can usually be divided into a rapid phase on the thermal timescale of the primary, followed by a slow phase on the much longer nuclear timescale. The fast phase of mass transfer proceeds until the primary regains thermal equilibrium, i.e., when its equilibrium radius becomes smaller than its Roche radius.

For Case A mass transfer, the orbit widens and the mass-transfer rate falls as the mass ratio of the primary to the secondary $q = \frac{M_2}{M_1}$ approaches unity. Beyond this time the donor star has become the less massive star in the system; in other words, the mass ratio has been reversed. During the rapid mass-transfer phase, both stars are out of thermal equilibrium: the primary is somewhat less luminous due to mass removal, while the secondary is somewhat more luminous as a result of accretion. The mass-transfer rate is also sensitively dependent on the mass ratio of the secondary star to the primary star, $q = \frac{M_2}{M_1} < 1$, with increasing rates for lower values of mass ratio q.

The second RLOF occurs at 10.635 Myr when the envelope of the primary star expands due to hydrogen shell burning during the helium core contraction phase. The resulting high mass-transfer rate (i.e., $\dot{M}_R \sim 1.9953 \times 10^{-4}\,M_\odot$ yr^{-1}) occurs again on the Kelvin–Helmholtz timescale. The primary star loses most of its hydrogen envelope, exposing its helium core of $3.5\,M_\odot$ with a small amount of hydrogen envelope $M_{\rm H} = 1.1\,M_\odot$. The luminosity $\log L/L_\odot$ increases from 4.52 to 4.72 accordingly. During this phase of mass transfer, the orbital separation increases significantly. Although the star remains compact ($R \sim 1.56\,R_\odot$) at the termination of the second mass transfer, the helium shell burning can be activated after core helium exhaustion. This leads to the expansion of the envelope up to $\sim$6.3 $R_\odot$ during core carbon burning.

Case B mass transfer in massive binaries B7 with orbital periods of $\sim$10 days is similar to Case A mass transfer in many respects. Because the envelope of the primary star is radiative, the mass transfer starts with a rapid, thermal-timescale phase

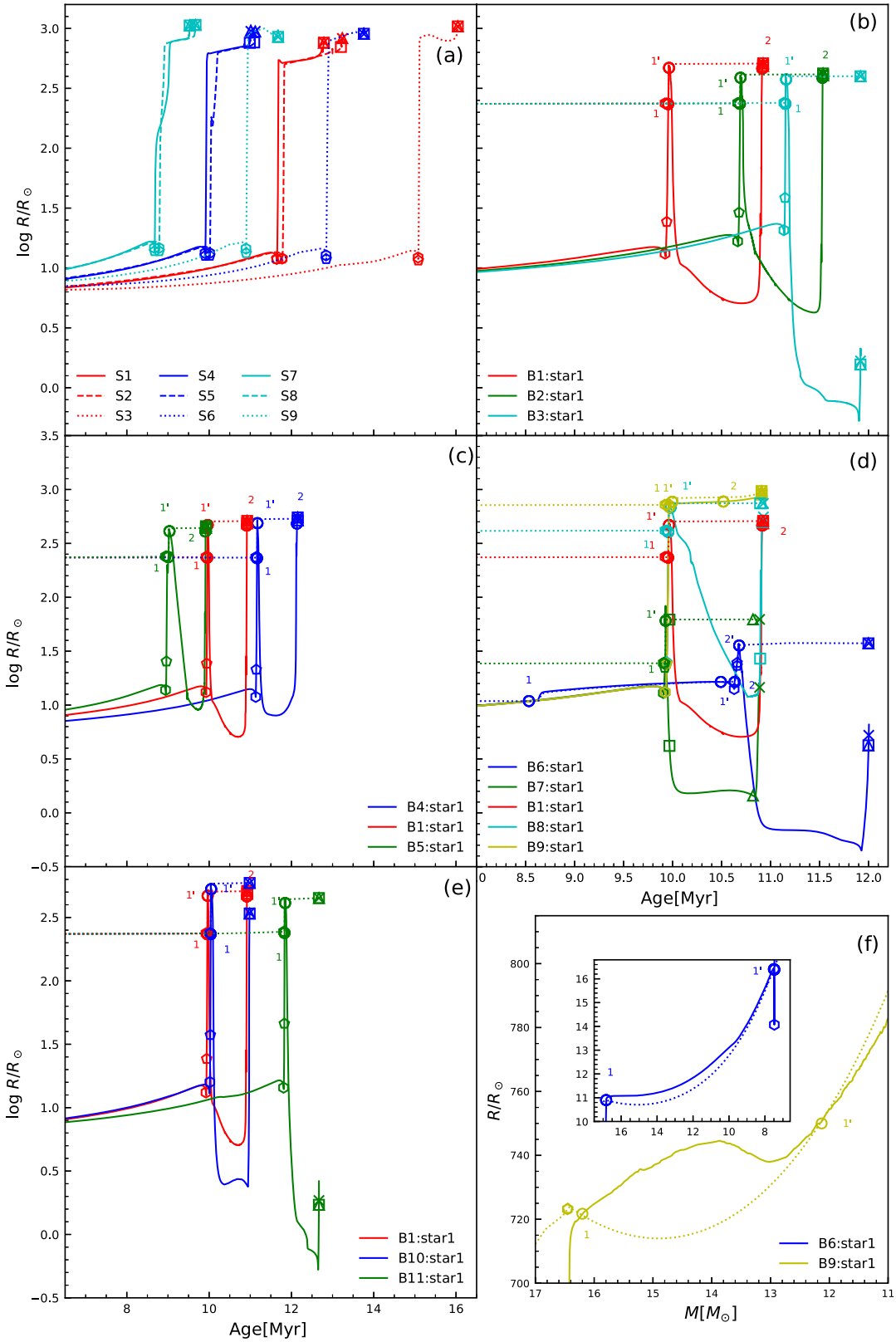

Figure 6. The evolution of photospheric radii as a function of evolutionary age. (a) For single stars with different initial masses and rotational velocities. (b) For primary stars with different overshoot parameters in a binary system with an initial $P_{\rm orb} = 300$ days. (c) For primary stars with different initial metallicities in a binary system with an initial $P_{\rm orb} = 300$ days. (d) For primary stars in a binary system with different initial orbital periods. (e) For primary stars in a binary system with an initial $P_{\rm orb} = 300$ days but with different initial rotational velocities. (f) The evolution of photospheric radii as a function of stellar mass in binary systems B6, with an initial $P_{\rm orb} = 300$ days, and B9, with an initial $P_{\rm orb} = 1600$ days. The dotted lines correspond to the evolution of the corresponding Roche lobe.

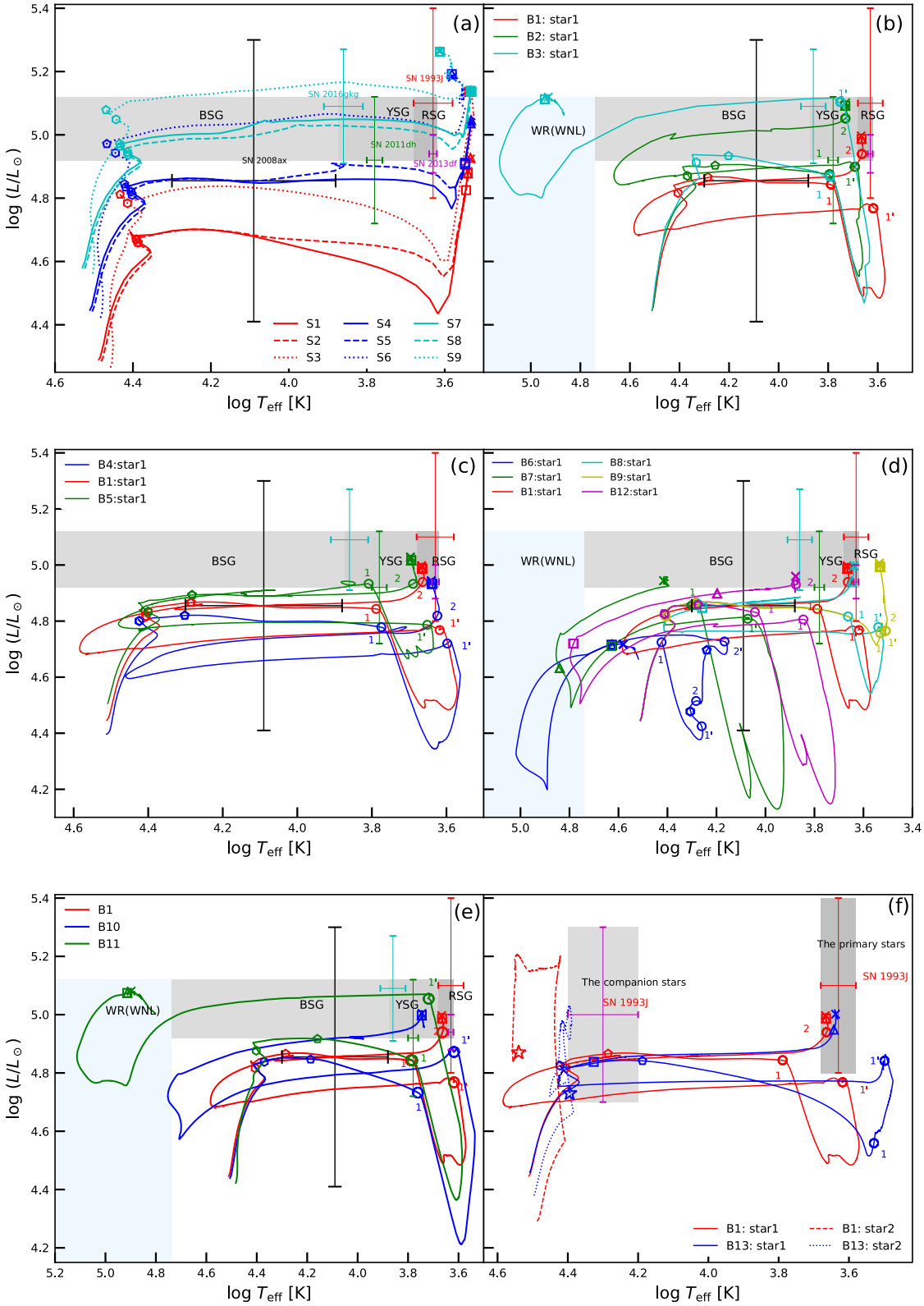

Figure 7. Evolutionary tracks of the stars on a HR diagram. (a) For single stars with different initial masses and rotational velocities. (b) For primary stars with different overshooting parameters in a binary system with an initial $P_{\rm orb} = 300$ days. (c) For primary stars with different initial metallicities in a binary system with an initial $P_{\rm orb} = 300$ days. (d) For primary stars in a binary system with different initial orbital periods. (e) For primary stars in a binary system with an initial $P_{\rm orb} = 300$ days but with different initial rotational velocities. (f) The evolution of the theoretical B1 and B13 models. The observational regions of two component stars for the SN 1993J progenitor are marked in the HR diagram. Observations for various types of SNe IIb are indicated in different shaded regions (Gilkis & Arcavi 2022). Five Type IIb SNe are marked in the HR diagram and their observations are from Sravan et al. (2020).

during which the mass ratio is reversed. An important difference is that since the donor star is more extended it therefore has a shorter thermal timescale compared to Case A mass transfer in model B6, and the mass-transfer rates are correspondingly larger during this phase. Moreover, the primary star is itself in a rapid phase of evolution when it passes through the Hertzsprung gap. It is out of thermal equilibrium and expands on the timescale at which its core contracts. As a consequence, after mass ratio reversal mass transfer continues on the expansion timescale of the primary, only slightly slower than the thermal timescale. Therefore there is a lack of slow-phase mass transfer as in Case A mass transfer. Mass transfer continues at a fairly high rate until most of the envelope has been removed. The evolutionary track forms a loop in the HR diagram during the mass-transfer phase, and the maximum transfer rate coincides with the minimum luminosity of the donor star (see Figure 7). The decrease of the luminosity during mass transfer is caused by the large thermal disequilibrium of the primary star. A primary star with the radiative envelope shrinks in response to mass loss and has to expand again to reach thermal equilibrium. This requires the absorption of the thermal energy, so that the surface luminosity during thermal-timescale mass transfer is much smaller than the nuclear luminosity provided by the helium-burning shell.

When central helium is ignited in the core, the mass transfer via RLOF ceases. The primary star contracts and detaches from its Roche lobe. This occurs when the primary is almost a bare helium core with $M_{\rm He} \sim 4.15\,M_{\odot}$ and a thin hydrogen-rich layer $\sim$0.75 $M_{\odot}$. The primary shifts to a position close to the helium main sequence in the HR diagram. The remnants of Case B mass transfer are in a long-lived phase of evolution: these are binaries consisting of an almost bare helium-burning core primary and a more massive main-sequence companion star. Mass transfer via RLOF will widen their orbits significantly. Observed counterparts of this evolution phase among massive systems are the WR+O binaries, consisting of a WR star and a massive O-type star.

A common prescription for the largest rates of RLOF is to assume that the mass transfer is limited by the thermal timescale of a massive star with a radiative envelope. This implies that the mass-transfer rate is likely to be highest for more massive and more luminous stars, which have short thermal timescales. The thermal timescale can also decrease as the star evolves. This indicates that the mass-transfer rate via RLOF is higher for wider systems, in which the donor star is more evolved. Mass-loss rates can be of order $2.4 \times 10^{-2}\,M_{\odot}\,{\rm yr}^{-1}$ for model B9 with an initial $P_{\rm orb} \approx 1600$ days. The main reason is that the adiabatic response of the donor is unable to keep it within its Roche lobe, leading to ever-increasing mass-transfer rates (Ritter 1988; Wellstein et al. 2001). Mass transfer accelerates to a timescale in between the thermal and dynamical timescales of the donor. Stars with deep convective envelopes, i.e., giants or RSGs, tend to expand or keep a roughly constant radius (i.e., the adiabatic mass–radius exponent $\zeta_{\rm ad} = \left(\frac{d\log R}{d\log M}\right)_{\rm ad} \leqslant 0$) when they lose mass adiabatically. This fact implies that the response to the mass transfer of a convective envelope is very different from that of a radiative envelope.

The Roche lobe radius shrinks when the mass is transferred from a more massive to a less massive star (see Figure 6(f)). The response to mass loss via RLOF can cause the donor to overfill its Roche lobe by an ever larger amount and cause runaway mass transfer. The maximum mass-transfer rate for Case C is the highest among the three cases of mass transfer. However, as the orbital period increases, the total amount of mass transfer via RLOF decreases. This indicates that the duration of RLOF becomes shorter in systems with an initially longer orbital period. When the envelope of the primary star expands, the second RLOF event happens at 10.519 Myr. The radius cannot expand because it is restricted by the Roche lobe. Finally, the primary has a helium core mass with $M_{\rm He} \sim 4.95\,M_{\odot}$ and a thick hydrogen-rich layer $\sim$1.87 $M_{\odot}$. Therefore, this kind of mass transfer cannot give rise to Type IIb SNe due to the existence of a thick envelope.

3.3.4. The Effect of Rotation

From Figure 5(d), one can see that the maximum rate of mass transfer via RLOF is also related to the rotation. One can see that rapid rotation can favor the maximum mass-transfer rate. However, the total amount of mass transfer via RLOF reduces with the increasing of rotational velocities. Rotation can delay the beginning of Case B mass transfer. There are three main reasons. First, rotational mixing can prolong the lifetime of the main sequence. Second, the orbital separation can be widened by the angular momentum transformation because more spin angular momentum can be transferred to the orbit. Third, rotation-enhanced stellar winds can also widen the orbital separation.

3.4. Stellar Radii and Evolution in the Hertzsprung–Russell Diagram

3.4.1. The Effect of Rotation

Figure 6(a) shows the photospheric radii for nonrotating and rotating single stars as a function of evolutionary age. One can see that from the beginning of evolution, an increase in rotational speed leads to a decrease in radius. It can be understood that the star receives a small gravitational acceleration because of the sustaining effect of the centrifugal force and behaves like a nonrotating star with a slightly lower mass. The central temperature is smaller and the corresponding central density is larger. This results in a decrease in both luminosity and radius. Massive stars expand more as they cross the Hertzsprung gap and ignite helium as an RSG while their radii swell slightly. The rotation effects are almost unnoticeable in the evolution of the radius after the main sequence because of the rapid expansion of the hydrogen envelope.

However, the rapidly rotating star S9 can experience very strong mass loss via stellar winds and its hydrogen-rich envelope can be removed when the core helium is ignited. The radius decreases and the star slightly shifts toward a WR star. A massive single star ($\sim$19 $M_{\odot}$) with an initial velocity of 400 km s^{-1} can approach the inferred luminosity and effective temperature of a Type IIb progenitor star. This star finally explodes as a Type IIP SN.

Figure 7(a) shows the evolutionary tracks in a HR diagram for nonrotating and rotating single stars. The effective temperature behaves as $T_{\rm eff} \propto M^{0.5-0.6}$ at the onset of evolution. Therefore, the effective temperature increases with the stellar mass. For a star with a moderate initial rotational velocity $v_{\rm ini} < 200\,{\rm km\,s^{-1}}$, the increase of the stellar wind with respect to the nonrotating case is limited. Rotational mixing merely plays a minor role in decreasing the opacity of the envelope. These models can maintain the star in the RSG state

throughout the whole core helium-burning phase. However, an efficient rotational mixing in model S9 can increase the size of the helium core significantly and the post-main-sequence luminosity of the fast rotating star is higher, by approximately a factor of ∼2.5 than that of a nonrotating counterpart S7. Therefore, the post-main-sequence luminosity of the rapidly rotating star is higher than its nonrotating counterpart. The enhanced mass loss by rotation in model S3 implies that tracks for the stars do not attain as far to the right of the HR diagram as they do for the nonrotating star S1. Furthermore, the star S9 with higher rotational velocities shifts its color earlier from the red part of the HR diagram after the core helium exhaustion than the model S7, which does not include rotation. The star terminates its evolution within the different regions of the HR diagram that have been defined by various types of SN IIb progenitors. The rotating model S9 can approach the observed effective temperature of the RSG-type SN IIb. However, the luminosities of SN IIb are in the range of $\log L/L_{\odot}$= 4.92–5.12. The final luminosity of the model S9 is beyond the scope of Type IIb observations.

Therefore, less massive stars (i.e., $M < 19\,M_{\odot}$) with higher rotational velocities are prone to form Type IIb SNe. Furthermore, we also note that blueward excursion can be increased by rotation in the binary system (see Figure 7(e)).

3.4.2. The Effect of Convective Overshoot

One can see in Figure 6(b) that convective overshooting from the core evidently provides a larger reservoir of available nuclear fuel during the main sequence, and consequently produces an increase of the effective temperature and the luminosity after the RSG stage. Hence the radius of a star slightly decreases at a given luminosity for larger overshooting. During helium burning the star has a higher overshoot parameter and a smaller radius because a larger amount of the hydrogen envelope has been removed in model B3. At a smaller hydrogen envelope mass $M_{\rm H} < 0.1\,M_{\odot}$, a higher luminosity is always associated with a smaller radius in model B3. The radius remains smaller than it is at the tip of the giant branch. Before the core helium exhaustion, the radius of model B3 can display a significant expansion because of the existence of a thick helium envelope. A double-peaked light curve has been observed in SN 1993J. The light curve shows a rapid decline during 1 to 3 days after an initial peak, which is a consequence of cooling after the shock breaks out from the surface. The duration of the cooling phase is mainly dominated by the radius of the progenitor. More compact sizes of the progenitor, as in WR stars, give rise to faster declines than extended progenitors, such as RSG stars. The main reason is that an extra amount of energy is needed to expand a more compact structure.

Figure 7(b) illustrates a HR diagram of three models with different convective overshoot parameters in the binary system. The convective overshoot is important to increase the luminosity on or after the main sequence and thereby stellar winds can also be increased. When the hydrogen starts to become exhausted in the core, a thin hydrogen-burning shell begins to take shape and moves outward. This leads to a subsequent expansion and cooling of the stellar envelope. The star B3 with larger overshooting rapidly moves to the redward in the HR diagram and becomes an RSG in comparison with the model B1 with smaller overshooting. This is the so-called "mirror effect." The low temperature from the expansion significantly increases the envelope's opacity at the RSG phase, which can make it easier for photons to be caught by the outer envelope, leading to increased radiation pressure and stronger line-driven winds. Moreover, the outer envelopes are also less tightly bound, since the radius is now several hundred solar radii or larger and the gravitational potential becomes shallow. Both of these effects enormously reinforce the mass loss and will result in a loss of a significant part of the outer envelope.

During the mass-transfer phase via RLOF, the stars lose most of their hydrogen-rich envelopes on a thermal timescale. The mass-transfer phase proceeds at similar effective temperatures in three models. The main reason is that the size of the Roche lobe is approximately the same in the three binaries. We have noted that the blue loop behavior is almost absent in all single stars in comparison with the binary system (see Figure 7(a)). We attribute this to the presence of a thick hydrogen envelope in the single stars. This implies that there exists a threshold for the hydrogen envelope mass, which can take the shape of the blue loop.

The inner layers with higher temperature can be exposed by RLOF. Actually, an evolution to the blue after the RSG appears only if the ratio of the core mass to the total mass can exceed a given limit of around 70%. This implies that the YSG or BSG will still have a hydrogen envelope that is comprised of a maximum of about 30% of the total mass. The hottest point of the blue loop in model B1 corresponds to the minimum in the stellar radius when the core helium drops at $Y_{\rm c,He} \sim 0.25$, after which the envelope starts to expand and the star approaches the red giant branch again when the core helium $Y_{\rm c,He} \sim 0.02$.

We also see that the blue excursion can be triggered earlier in B3 with larger overshooting than the B1 model with smaller overshooting. The reason is that the higher luminosity induced by larger convective overshooting can trigger stronger stellar winds after the RLOF. The donor star loses a large amount of hydrogen during the blue excursion phase when the WR wind of Nugis & Lamers (2000) is adopted. The remaining hydrogen envelope can be completely eliminated by strong winds. The binary model B3 will explode as a Type Ib SNe because the hydrogen envelope is less than 1% of the total mass.

3.4.3. The Effect of Metallicity

Figure 6(c) shows the radius as a function of evolutionary age at various metallicities. The radius is smaller at lower metallicity during the main sequence. There are two main reasons for this fact. First, because an extremely low metallicity implies a weaker CNO cycle, the nuclear reaction strongly depends on proton–proton (pp) chains to produce its nuclear energy at the beginning of its evolution. Since pp chains are much less sensitive to temperature than the CNO cycle, the star has to contract more to obtain a higher central temperature. Second, the opacity is lower and thus the envelope is more transparent at low metallicity. The radiative gradient $\nabla_{\rm rad} \propto \frac{\kappa {\rm P}}{T^4}$ is lower and the star remains more compact.

Before RLOF, we can see that the model with lower metallicity can display a larger expansion compared to the one with higher metallicity. The reason is that the residual hydrogen mass in the envelope is closely related to the stellar radius. The stellar radius generally decreases with the decreasing of the leftover hydrogen mass in the envelope. The progenitor radius of the Type IIb SNe ranges from $\sim 50\,R_{\odot}$ of the BSG progenitor to $\sim 600\,R_{\odot}$ of the RSG progenitor. One of the main parameters that can determine the final radius and

surface temperature of an SN IIb progenitor is the hydrogen envelope mass at the pre-SN stage. We note that the mass range of the hydrogen envelope for RSG-type SN IIb is $0.35\,M_{\odot} < M_{\rm H} < 0.5\,M_{\odot}$, $0.15\,{\rm M}_{\odot} < {\rm M}_{\rm H} < 0.35\,M_{\odot}$ for YSG-type SN IIb, and $\sim 0.033\,M_{\odot} < {\rm M}_{\rm H} < 0.15\,M_{\odot}$ for BSG-type SN IIb (see Table 1). Gilkis & Arcavi (2022) proposed that the Type Ib and Type IIb hydrogen mass threshold is $0.033\,M_{\odot}$. This can be approximately consistent with the previous estimates for the SNe IIb: $M_{\rm H} = 0.2-0.4\,M_{\odot}$ for SN 1993J and SN 2013df (RSG progenitor), $M_{\rm H} \simeq 0.1\,M_{\odot}$ for SN 2011dh (YSG progenitor), and $M_{\rm H} \simeq 0.06\,M_{\odot}$ for SN 2008ax (BSG progenitor).

Stars with equal masses on the ZAMS but with different initial metallicities have different pre-SN structures for a variety of reasons. Most importantly, if the amounts of mass loss are very low in the single stars, the pre-SN star, including its helium core, will be larger. Finally, it has a greater compactness (Sukhbold & Woosley 2014). We can see that the primary star in the binary system can deviate from this trend because the helium core can be reduced by RLOF. Moreover, low metallicity implies a smaller initial helium mass fraction and more hydrogen. The final helium core mass is sensitive to this and is reduced accordingly (see Figure 3(b)).

Figure 7(c) illustrates a HR diagram of three models at various metallicities. The stars with low metallicity become bluer compared with the counterpart with high metallicity. The central temperature is slightly higher at low metallicity because of the lower abundance of CNO, which can catalyze the nuclear reaction. When core hydrogen is exhausted, the star with low metallicity starts the central helium burning at the blue side of the HR diagram compared with the one with high metallicity.

Note that the primary star in three binaries can experience a second RSG phase when the helium becomes depleted in the core. Low metallicity reduces the energy generation of the CNO cycle. The more active hydrogen-burning shell in the high-metallicity case reduces the pressure on the helium core. The metal-rich model is hotter and more compact than the metal-poor model at core carbon exhaustion because the metal-poor model can retain more hydrogen envelope. Therefore, low-metallicity stars give rise to the slightly stripped Type IIb SNe, while higher metallicity stars are prone to producing Type Ib or Type Ic SNe.

The hydrogen envelope in SN IIb progenitors becomes thicker for lower metallicity stars, while the corresponding opacity becomes smaller. As these two effects compensate each other, the radii of the Type IIb progenitor for both low- or high-metallicity models B4 and B5 are found to be very similar (see Table 1). The more compact supergiant envelope in model B5 places greater pressure on the helium core therein and can affect its subsequent evolution. It can determine if the progenitor is an RSG or a YSG. For example, the model B4 explodes as an RSG-type SN IIb progenitor, whereas model B5 ends as a YSG-type SN IIb progenitor.

3.4.4. The Effect of Orbital Period

Figure 6(d) shows radius as a function of evolutionary age at various orbital periods. The radial evolution becomes very distinct, with a monotonic increase of the radius for single stars until a maximum of $\sim 10^3\,R_{\odot}$ is reached. A nonmonotonic increase of the radius occurs in the binary system because the thermal equilibrium is broken by the presence of RLOF. The more hydrogen stripped from the envelope, the larger the radius shrinks during the RLOF. When the mass transfer via RLOF goes down, the star gradually restores thermal equilibrium and its radius gradually increases. Actually, the radius can be greatly changed by the complication of binary interaction: the presence of a thin hydrogen envelope in some of the binary models leads to a more extended envelope than in the corresponding single helium star models in the absence of a hydrogen envelope (Yoon et al. 2017). The composition of the envelope also has an important impact on the evolution of the effective temperature. The presence of hydrogen in the envelope of the extended progenitor can greatly reduce the effective temperature of the progenitor. One can notice that single-star progenitors tend to have larger radii than binary-star progenitors. For example, the radius of the binary-star SN progenitor model B1 is $851\,R_{\odot}$, while the radius of its single-star counterpart S4 is $933\,R_{\odot}$. There are two main reasons. First, the stellar radius in binary systems is limited by the Roche lobe. Second, a smaller residual hydrogen envelope can be retained in the binary system due to mass transfer via the RLOF.

SNe IIb progenitors with smaller (larger) envelope masses are more compact (extended) and hot (cool). The ultrastripped primaries are believed to be very hot objects, emitting the majority of their photons in the extreme UV, and can remain hidden by their companions. The slightly stripped donors would be significantly cooler and more visible in their evolution (Götberg et al. 2017). A more progressive stripping process in an initially tighter system can cause the star to evolve toward a hydrogen-deficient WR star. The mass-loss rate just before the SN explosions contains important information about their evolutionary paths. The mass-loss property is reflected in the density of circumstellar matter. The radii of Type IIb SNe covers the region from $\sim 50\,R_{\odot}$ of the BSG progenitors to $\sim 600\,R_{\odot}$ of the RSG progenitors. Maeda et al. (2015) have shown that there is a close relationship between the mass-loss rate of stellar winds and the progenitor radius prior to the explosion. They demonstrated that more extended progenitors ($\sim 600\,R_{\odot}$, e.g., 1993J and 2013df) have a higher mass-loss rate up to $\sim 10^{-5}\,M_{\odot}\,{\rm yr}^{-1}$, while less extended progenitors ($\sim 200\,R_{\odot}$, e.g., SN 2011dh) have a moderate mass-loss rate ($\sim 3 \times 10^{-6}\,M_{\odot}\,{\rm yr}^{-1}$). Ouchi & Maeda (2017) interpreted that the less extended Type IIb SN progenitor has not only a smaller remanent envelope mass to transfer but also a larger equilibrium index value, $\xi_{\rm eq} = \left(\frac{\partial \log R}{\partial \log M}\right)_{\rm eq}$, which denotes the variation in primary radius in response to the reduction of the envelope mass, assuming that this mass loss proceeds slowly enough to maintain the primary in thermal equilibrium. The larger value of $\xi_{\rm eq}$ indicates that the progenitor shrinks faster in response to the mass loss. However, van & van der Veen (2005) reported that the mass-loss rate via stellar winds can reach as high as $\sim 10^{-4}\,M_{\odot}\,{\rm yr}^{-1}$ from some RSG stars. It may also be an alternative interpretation that the strong mass loss for the more extended progenitor can be understood by a post-RLOF stellar wind of RSGs in the model B1. The radius of the primary in model B1 can attain a value of $478\,R_{\odot}$ and its stellar wind has a value of $2.58 \times 10^{-6}\,M_{\odot}\,{\rm yr}^{-1}$ (RSG progenitor of SN IIb). These theoretical results are approximatively consistent with observations of the Type IIb SNe 1993J (see Table 2; Sravan et al. 2020).

The thin envelope of an SN IIb has a very low mass compared to the envelope of an SN IIP. This SN IIb thin envelope is capable of soaking up a lot of energy from the SN shock, leading to the subsequent strong or rapid cooling emission. The large radius ($\sim$600 $R_{\odot}$) of SN 1993J is due to a thin extended hydrogen envelope around the progenitor and should have important impact on shock breakouts and bolometric light curves. The extended model gives rise to an apparent peak at the early stage (at the time of 5 days after the SN explosion) of the observed bolometric light curves of the SN IIb while the compact progenitor shows a much smaller bulge. The main difference is due to the extra amount of energy required to expand a more compact structure (Bersten et al. 2012).

Figure 7(d) illustrates the evolution of several models with various initial orbital periods in a HR diagram. Models with different initial orbital periods can give rise to the blue, yellow, and red supergiant SN IIb progenitors. Whether a star explodes as an RSG or BSG, and how much hydrogen envelope remains, depends on the mass loss via stellar winds or the RLOF in the binary system. The extended blue loop can be greatly influenced by the enhanced mass loss via RLOF. The effective temperature gradually reduces with the increase of the size of the radius and the initial orbital period. The primary in an initially tighter system is hotter and more compact than the one in a wider system because an initially wider system can retain more hydrogen in its envelope, which allows it to expand greatly. The position in the HR diagram of the endpoint of the evolution heavily depends on the leftover mass of the hydrogen envelope. If the hydrogen envelope contains more than about 5% of the initial mass, the star evolves into an RSG star with a lower effective temperature at the pre-SN stage (Meynet et al. 2015). If the hydrogen envelope remains less than 1% of the total mass, the star becomes a BSG or a WR star. The primary star in the wide system retains a significant hydrogen layer after RLOF, which can sustain a hydrogen-burning shell while the one in the tight system loses its hydrogen-rich envelope earlier due to an ultrastripped RLOF. The hydrogen shell burning governs the nuclear luminosity during the time of helium exhaustion, and this results in a local maximum in the radius. The inflated hydrogen envelope of the supergiant progenitor has an important impact on the early-time light curves of SNe IIb during the shock-cooling phase. An inflated hydrogen envelope can contribute to sustained high luminosity.

The wind mass loss of a single star with mass $<20\,M_{\odot}$ is not strong enough to completely expel the envelope (see Figure 5(a)). Instead, for a less massive star ($<20\,M_{\odot}$) to become a SE SN, a significant mass transfer in a close binary system is needed. In this case, the SE SN has lower mass. RLOF can avoid the redward evolution after the main sequence in the initially tighter systems B6 and B7.

The pre-explosion photometry of the progenitor is critical for the evolution and final appearance of an SN IIb and its companion star. To date, a total of five Type IIb SN progenitors have been identified in pre-explosion imaging, from SN 1993J to the more recent SN 2016gkg. Some observational evidence suggests the presence of its companion near the progenitor stars of SN 1993J, SN 2001ig, and SN 2011dh. The observational position of two component stars in the HR diagram can also provide us with a good target to construct the theoretical model and the evolutionary properties. At the time of SN explosion, the primary star in model B1 fits well with the the pre-explosion observations. However, the location of the companion star of SN 1993J in the HR diagram is in approximate agreement with observations. The luminosity of the secondary practically match the observations, but the star is too blue (see Figure 7(f)). The secondary in our model is shifted to a higher effective temperature by just $\Delta \log T_{\rm eff} \simeq 0.14$. Stancliffe & Eldridge (2009) have claimed that it is extremely difficult for the secondary star to attain the observational position in the HR diagram. The position indicates that the secondary star appears as an overluminous B supergiant and is extremely close to (or just beyond) the right side of its main-sequence band. Its position predicted by the theoretical model is extremely sensitive to the value of the accretion efficiency β (Benvenuto et al. 2013). Both the effective temperature and luminosity of the companion star of SN 1993J can be reduced by a smaller accretion efficiency. They demonstrated that this can be done only in a very narrow range in initial masses and periods. Stancliffe & Eldridge (2009) have presented such that, if mass transfer is conservative, the right location of the secondary in the HR diagram can be reproduced by a system consisting of a $15\,M_{\odot}$ primary and a $14\,M_{\odot}$ secondary in an orbit with an initial period of 2100 days. However, they made use of a high-metallicity model with $Z = 0.04$. We simulate the system of SN 1993J to be composed of a $16\,M_{\odot}$ primary and a $15\,M_{\odot}$ secondary with an initial orbital period of 1100 days. The metallicity is $Z = 0.04$ and the accretion efficiency is adjusted to a value of $\beta = 0.15$. The final evolutionary positions of the two components in the HR diagram are in good agreement with the observations (see Table 2 and Figure 7(f)). In model B12, the luminosity and the effective temperature of the primary have values of $\log L/L_{\odot} = 4.91$ and $\log T_{\rm eff} = 3.88$, respectively. The observations of the SN 2008ax progenitor implies that the luminosity and the effective temperature of the primary are $\log L/L_{\odot} = 4.42 - 5.3$ and $\log T_{\rm eff} = 3.88 - 4.3$, respectively (Sravan et al. 2020). These theoretical results can also be consistent with the observations of SN 2008ax (BSG progenitor of SN IIb).

3.5. Carbon Profile at Core Carbon Exhaustion

3.5.1. The Effect of Convective Overshoot

Figure 8(a) shows the mass fraction of carbon as a function of the Lagrangian mass for nonrotating and rotating single stars at core carbon exhaustion. The CO core mass, which scales with the mass of the helium core, increases with the initial mass of the star at all metallicities. For example, the CO core mass is $2.853\,M_{\odot}$ for model S4 while it is $3.418\,M_{\odot}$ for model S7. One can see that overshooting governs the final mass of the CO core. A higher overshoot parameter can result in a larger final CO core mass. The growth of the helium-burning core overshoot can bring about an additional supply of helium above the core that favors the formation of a larger CO core at core helium exhaustion. Actually, all single stars and the peeled primary stars in our calculations display similar density profiles in the iron core (i.e., $M < \sim 1.6\,M_{\odot}$). However, the star shows a shallower drop of the density profile above the iron core for the more massive helium core. The local density tends to be higher while the central core has a higher temperature.

An important effect is that the increase of overshooting leads to a lower ratio of carbon to oxygen at the end of helium core

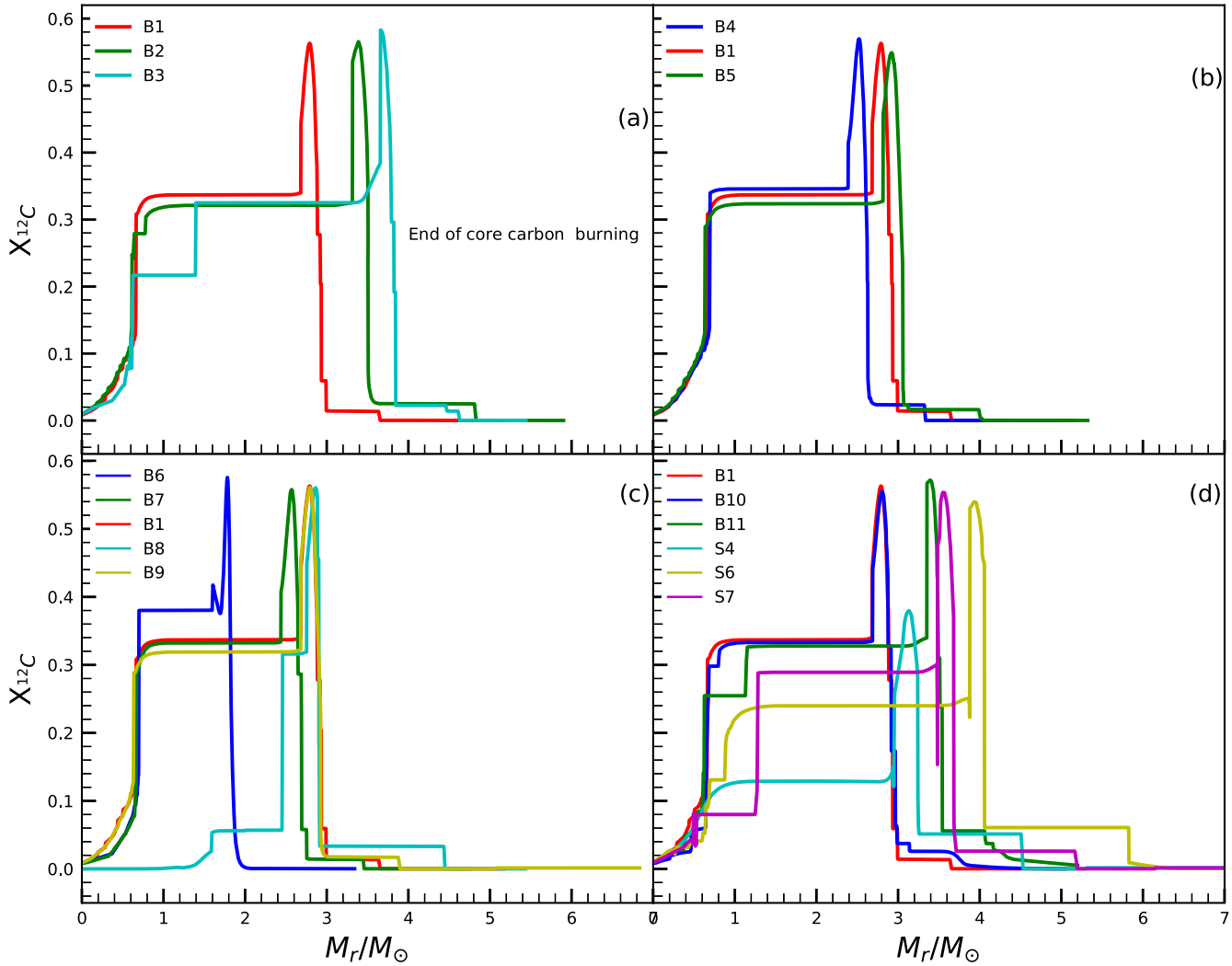

Figure 8. Carbon mass fraction as a function of the mass coordinate at the moment of core carbon depletion. (a) For primary stars with different overshoot parameters in a binary system with an initial $P_{\rm orb} = 300$ days. (b) For primary stars with different initial metallicities in a binary system with an initial $P_{\rm orb} = 300$ days. (c) For primary stars in a binary system with different initial orbital periods. (d) For primary stars with different initial orbital periods and for single stars with different initial masses and rotational velocities.

burning, which can have a strong impact on the strength of subsequent carbon burning and the final size of the iron core. For a high carbon abundance in the model with a smaller overshoot parameter, the phase of convective carbon shell burning may proceed longer, typically leading to smaller carbon-exhausted cores. This outcome in turn produces smaller iron cores with steeper density gradients outside the iron core and results in a pre-SN structure that more easily produces a successful SN (Limongi & Chieffi 2018). Furthermore, the formation of a larger convective core induced by overshooting slows down the contraction of the core as well as its heating.

It can be noticed that at the mass coordinate of $1.0\,M_\odot$ the central carbon mass fraction reduces with increasing of the overshoot parameter. Generally, the mass fraction ^{12}C left by the core helium burning decreases with the CO core mass. This is because the star with a larger convective overshooting has a higher reference core mass. This condition favors the rate of alpha capture onto carbon over the triple-alpha process. Therefore, carbon is destroyed more efficiently in the larger core induced by the convective overshoot and the mass fraction of oxygen is higher in the enlarged core. This contributes to a faster outward shift of the carbon-burning shell and a more compact core of the star (Chieffi & Limongi 2013).

3.5.2. The Effect of Metallicity

Figure 8(b) shows the mass fraction of carbon as a function of the Lagrangian mass for nonrotating binary models with different metallicities at the end of the core carbon-burning phase. In fact, mass loss in the more massive star is strong enough to reduce substantially the total mass and therefore to reduce the hydrogen convective core during the main sequence. As a consequence, the helium core mass is smaller than it would be in the case of weak mass loss. Therefore, a strong mass loss in a star with high metallicity will drive evolution toward a smaller CO core in contrast to a model with low metallicity.

However, RLOF can make the low-metallicity primary star B4 transfer more hydrogen envelopes to the companion. Therefore, the CO core mass in the low-metallicity star becomes smaller due to RLOF. The star tends to behave as a lower mass star and evolves toward lower central temperature and higher central density. Such an occurrence has five

outcomes. First, the helium convective core shrinks progressively in mass and leaves a zone with variable chemical composition. Second, the lifetime of core helium burning goes up accordingly. Third, the total luminosity progressively falls down and then the star shifts downward in the HR diagram. Fourth, the local density above the iron core tends to be higher in an initial high-metallicity circumstance while the central temperature becomes larger. The mass fraction of ^{12}C at the time of core helium exhaustion becomes larger than it would be in a high-metallicity binary system. Finally, the CO core at core helium exhaustion is smaller than it would be in a high-metallicity binary system. Generally speaking, stellar compactness at the pre-SN stage increases with the CO mass. Therefore, it is found that a primary star with low metallicity is easier to explode. As a consequence, we expect these models to produce smaller remnant masses and, eventually, to give rise to faint and failed SNe.

3.5.3. The Effect of Orbital Period

Figure 8(c) shows the carbon profiles for primary stars with different orbital periods in a binary system at the time of core carbon exhaustion. For a given initial mass, the final CO core mass may originate from different initial orbital periods. As can be seen, a smaller CO core can be induced by RLOF in an initially tighter system B6. The local density above the iron core tends to be smaller in this system while the central temperature becomes lower.

We also find that a higher central carbon abundance can be reached in this system. A hydrogen-burning shell can be extinguished because of RLOF. This leads to a smaller helium core and a higher ratio of carbon to oxygen at the end of carbon core burning, which have an important impact on the strength of subsequent carbon burning and the final size of the iron core (Brown et al. 2001). The bolometric luminosity of the SN progenitor can mainly be resolved by helium shell burning, which is in turn largely resolved by the mass of the CO core. However, the strength of the secondary carbon convective shell progressively weakens because the fraction of carbon left after the core helium exhaustion inversely scales with the CO core mass. The final degree of the core compactness of a star can be increased because it heavily depends on the formation and development of the various carbon convective episodes (Chieffi et al. 2000; Limongi & Chieffi 2009).

3.5.4. The Effect of Rotation

Figure 8(d) illustrates the carbon profiles of single stars and primary stars in a binary system for different rotational velocities at the time of core carbon exhaustion. Rapid rotation can increase the mass of helium and CO cores in both single stars and binary systems. The greater the initial rotational speed, the greater the helium and CO core mass. The corresponding central density tends to be higher. Therefore, rotational mixing can significantly reduce the mass fraction ^{12}C at core helium exhaustion. Rotation can also continuously mix the helium outside the helium-burning region and give rise to more ^{12}C. At a given initial rotational velocity, the mass of the CO core in a single star is larger than in a binary system. For example, the CO core mass is 3.16 $M_{\odot}$ for model B11, while it is 2.62 $M_{\odot}$ for model S6. The main reason is that RLOF can extinguish the hydrogen-burning shell, which may contribute an amount of helium to the helium core. For a given initial mass, rotating models behave like more massive stars and therefore they end their life with more compact structures.

4. Discussion

There is an unsolved, long-standing problem that the observed rates of Type IIb SNe seem to be much higher than the one which is predicted by binary evolution, in particular Type IIb SNe with RSG/YSG progenitors. Claeys et al. (2011) have presented that binary evolution predicts roughly 0.6% of all core-collapse SNe to be Type IIb SNe, about a factor 5 lower than the observed rate. In fact, they restrained the parameter spaces at solar metallicity to the initial primary mass of 15 $M_{\odot}$, initial secondary masses 10–15 $M_{\odot}$, and initial orbital periods 800–2100 days. Because of their limited parameter space coverage, they were not able to obtan robust relative rates. Another limitation is that they restrict their analysis to progenitors that explode with 0.1–0.5 $M_{\odot}$ of residual hydrogen envelope. The low mass limit of 0.1 $M_{\odot}$ excludes the group of more compact SN IIb progenitors obtained from theoretical models and it can be significantly reduced by recent observations.

Actually, this fraction increases if the companion star can accrete only a small fraction of the transferred mass via RLOF, and if the mass outflow carries relatively low angular momentum. If more material can escape from the binary system and take along its orbital momentum, this will cause the orbit to shrink faster, promoting a parameter space for the evolution of contact or unstable mass transfer. This evolutionary pathway might increase the probability of the CEE channel to produce Type IIb SNe and was not included in the calculation of Claeys et al. (2011). A smaller accretion efficiency can broaden the orbit and therefore the Roche lobe. This results in smaller mass-transfer rates via the RLOF and therefore larger hydrogen envelope masses of the donor at the time of explosion. A smaller accretion efficiency tends to generate stable mass transfer and leads to more Type IIb SNe than Type Ib SNe. Therefore, lower mass-transfer efficiencies are also favorable for the production of SNe IIb with RSG/YSG progenitors.

Moreover, if post-RLOF wind is lower than usual, it can greatly increase the rates that are predicted by binary evolution. Gilkis et al. (2019) commented that the wind mass-loss rate derived by Vink (2017), instead of the rate by Nugis & Lamers (2000), greatly shifts binary progenitor models for core-collapse SNe over a large initial parameter space from Type Ib to Type IIb. The mass-loss rate is expected to be smaller at lower metallicites, and thus Yoon et al. (2017) presented that there would be even more Type IIb SNe relative to Type Ib SNe.

In this paper, we intend to expand the parameter space for Type IIb SN progenitors using detailed binary evolutionary calculations. With a smaller overshoot parameter, the stars have smaller core masses and hence are less luminous, with smaller radii. However, the final remnant masses tend to be similar to their counterpart with a larger overshoot parameter. As a result, these stars have much smaller final helium core masses and they lose less of their envelopes accordingly, retaining larger amounts of hydrogen at the point of explosion. This evolution may be in favor of the formation of SNe IIb with RSG/YSG progenitors.

Rotation is thought to play a critical role in massive star evolution, and rapidly rotating stars are even predicted to

evolve chemically homogeneously due to the high efficiency of rotational mixing (Maeder & Meynet 1987; de Mink et al. 2009; Song et al. 2016). The star evolves blueward without experiencing the RSG phase. This evolutionary pathway greatly reduces the mass of the hydrogen envelope and significantly increases the production rate of Type IIb or Type Ib SNe. Moreover, rotationally enhanced mass-loss rates can also reduce the minimum mass required for a single star to remove its hydrogen envelope (Meynet & Maeder 2003). Mass loss by line-driven winds is closely related to the chemical abundances and the luminosity. Therefore, rotation mixing can enhance the surface helium fraction and the luminosity, and this also increases the rate of SN IIb with RSG/YSG progenitors from single stars.

Sravan et al. (2018) have found that it is very difficult to account for the rate of Type IIb SNe at solar metallicity. They take a ratio of Type IIb SNe of about 10%–12% in high-metallicity stellar populations and about 20% in low-metallicity populations. Therefore, the parameter space for binary SNe IIb rapidly increases with the decreasing of metallicity. This is because of evolutionary channels to SNe IIb via early Case B mass transfer that is only viable at low metallicity. In brief, a new statistical investigation is needed to compare binary models with the overall rates of different types of core-collapse SNe in future work.

5. Conclusion and Summary

In this paper, we investigate the evolution of stars that lose most of their hydrogen-rich envelopes because of interaction with companions. We consider binary systems with various convective overshoots, metallicities, initial orbital periods, and initial rotational velocities, and these physical factors are in favor of the formation of Type IIb SNe. We study how the internal structure and nucleosynthesis are connected with the evolution of the star. The main conclusions can be summarized as follows:

1. SN IIb show hydrogen lines in early spectra, while later spectra show helium lines but no hydrogen lines. They are believed to originate from core-collapse SNe with very thin hydrogen left in their outer envelopes. There are two stripping mechanisms for the formation of Type IIb SNe. These are strong line-driven winds from isolated massive stars and mass transfer via RLOF in binary systems. Stellar wind in the less massive stars' range within $M < 20\,M_{\odot}$ is too weak to give rise to Type IIb SNe because there exists a thick hydrogen envelope. Mass transfer via RLOF provides a promising channel for mass loss that is not solely regulated by the mass loss via stellar winds. Interacting binaries can therefore explain the existence of relatively low-mass progenitors of Type IIb SNe. Some initial parameters, such as rotational velocities, metallicity, overshooting, and orbital period, have important impacts on the RLOF and thus the formation of Type IIb SNe. A larger hydrogen envelope mass indicates a more extended radius and a lower effective temperature, and vice versa.
2. The faster the initial rotation rate, the greater the mass-loss rate of the stellar winds. Rapid rotation can decrease the low limit of the mass that can turn into a Type IIb SN due to rotationally enhanced helium cores and stellar winds. Initially, stellar luminosities are lower in rotating models because the effective gravitational acceleration can be reduced by the centrifugal force. Later, stellar luminosity is higher because the helium core can be enlarged under the influence of Eddington–Sweet circulation. The models with rotation have higher core temperature and lower central density due to more massive convective helium cores. Relatively low-mass helium stars usually experience a rapid expansion of the envelope during the core carbon-burning phase. Moreover, the opacity in the radiative envelope can be decreased by rotational mixing and the corresponding efficiency of the convective dredge-up can be reduced. Rotational mixing can enlarge the main-sequence lifetime. Rotational mixing is responsible for the transport of nuclear matter from the core to the surface. Surface chemical species of CNO processing can be changed in rotating models. Surface ^{4}He and ^{14}N are enhanced by rotational mixing while surface ^{12}C and ^{16}O can be decreased. Rotational mixing can affect the hydrogen abundance just outside the helium core, which in turn decreases energy generation from hydrogen shell burning. Rotating stars can produce larger CO cores and a greater compactness than their nonrotating counterparts.
3. Larger convective overshoot is very important for setting the larger size of the convective cores, especially for helium or carbon cores in the advanced evolution of massive stars. It also can increase the stellar luminosity, stellar winds, and lifetime in the main sequence. Moreover, overshooting can also decrease the minimum mass for the formation of Type IIb SNe. The larger convective overshooting develops a larger CO core and higher compactness than nonrotating stars. Larger overshooting can restrict the development of the dredge-up and there appears a smaller convective dredge-up region after core hydrogen exhaustion. In binary systems, the hydrogen-burning shell can be extinguished earlier in the model with the larger overshoot. Larger nitrogen enrichments can be reproduced by both RLOF and the subsequent strong WR winds.
4. Stars with different initial metallicities have different pre-SN structures. Most importantly, metallicity has an important impact on mass loss via stellar winds. If the amount of mass lost is very low, the helium core and the compactness of the pre-SN star will be larger. Moreover, low metallicity implies a smaller initial helium mass fraction and the final helium core mass can be reduced. Low metallicity decreases the energy generation of the hydrogen shell burning via the CNO cycle, and this decreases the boundary for the helium core. The opacity reduces with the decreasing of metallicity. The combined effects of opacity, energy generation, and mass loss determine whether the progenitor ends up as an RSG or a BSG. A primary star with lower metallicity is prone to generate a more compact blue progenitor and can retain less hydrogen mass during RLOF. The more compact radiative structure of the BSG envelope places greater boundary pressure on the helium core, which has an important effect on the subsequent evolution. A donor with higher metallicity tends to give rise to higher-effective-temperature SN IIb progenitors.
5. Compared with single stars, the primary stars in binary systems develop less massive helium and CO cores. This

is expected by the loss of mass due to mass transfer. As hydrogen is converted into helium in the core, the interior of the star becomes progressively less sensitive to variations in the total mass but more sensitive to the mass of the helium core. Close binary evolution should lead to a further stripping of the hydrogen envelope, and the formation of SN IIb is extremely sensitive to the initial orbital period. The effective temperature gradually decreases with increasing initial orbital period while the size of the radius goes up. This can be explained by the fact that less hydrogen is eliminated in the case of a binary with wider orbit. Systems in the range $\sim$10 days $< P_{\rm orb} <$ 700 days may turn into Type SNe IIb. A model with $P_{\rm orb} = 3.0$ days loses all of its hydrogen-rich envelopes and becomes a SNe Ib, whereas a system with initial $P_{\rm orb} >$ 700 days finally explodes as an RSG-type SNe IIP. A system with 300 days $< P_{\rm orb} <$ 700 days can give rise to an RSG-type SN IIb progenitor. The initial period of 300 days roughly separates the RSG-type SN IIb progenitors from the YSG-type progenitors. The binary system B7, with an initial $P_{\rm orb} = 30$ days, can produce BSG-type SN IIb progenitors. The primary star in a binary system may end its life as a compact BSG; this depends on the larger overshoot parameter and initial orbital period.

6. The mass fraction of ^{12}C left in the core when core helium is depleted can significantly affect the structure of the SNe progenitor. Generally, the mass fraction of ^{12}C left in the core after core helium burning falls with the increase of CO core mass. This can contribute to a faster outward shift of the ^{12}C-burning shell and make the core of the star more compact. The fraction of ^{12}C left heavily depends on the mass loss via RLOF, metallicity, overshooting, and initial rotational velocity. The remaining mass fraction of ^{12}C is higher in an initially tighter binary system with smaller overshooting, lower initial rotational velocities, and metallicity.

We are very grateful to an anonymous referee for the valuable suggestions and very insightful remarks, which have improved this paper greatly. This work was sponsored by the National Natural Science Foundation of China (grant Nos. 11863003, 12173010), the Swiss National Science Foundation (project number 200020-172505), and the Science and Technology plan projects of Guizhou province (grant No. [2018]5781). Y.Q. gratefully acknowledges the Science Foundation of University in Anhui Province (grant No. KJ2021A0106).

ORCID iDs

Andre Maeder https://orcid.org/0000-0001-8744-0444
Ying Qin https://orcid.org/0000-0002-2956-8367

References

Arnett, W. D., & Meakin, C. 2011, ApJ, 733, 78
Benvenuto, O. G., Bersten, M. C., & Nomoto, K. 2013, ApJ, 762, 74
Bersten, M. C., Benvenuto, O. G., Nomoto, K., et al. 2012, ApJ, 757, 31
Branch, D., Nomoto, K., & Filippenko, A. V. 1991, ComAp, 15, 221
Brott, I., de Mink, S. E., Cantiello, M., et al. 2011, A&A, 530, A115
Brown, T. M., Sweigart, A. V., Lanz, T., Landsman, W. B., & Hubeny, I. 2001, ApJ, 562, 368
Chevalier, R. A., & Soderberg, A. M. 2010, ApJL, 711, L40
Chieffi, A., & Limongi, M. 2013, ApJ, 764, 21
Chieffi, A., Limongi, M., & Straniero, O. 2000, in The Evolution of the Milky Way: Stars versus Clusters, ed. F. Matteucci & F. Giovannelli (Dordrecht: Kluwer), 417
Claeys, J. S. W., de Mink, S. E., Pols, O. R., Eldridge, J. J., & Baes, M. 2011, A&A, 528, A131
de Jager, C., Nieuwenhuijden, H., & van der Hucht, K. A. 1988, BICDS, 35, 141
de Mink, S. E., Pols, O. R., Langer, N., & Izzard, R. G. 2009, A&A, 507, L1
Dessart, L., Hillier, D. J., Livne, E., et al. 2011, MNRAS, 414, 2985
Eggleton, P. P. 1983, ApJ, 268, 368
Ekström, S. 2008, PhD thesis, Univ. Geneva, Astronomical Observatory
Endal, A. S., & Sofia, S. 1978, ApJ, 220, 279
Filippenko, A. V. 1991, in IAU Symp. 143, Wolf–Rayet Stars and Interrelations with Other Massive Stars in Galaxies, ed. K. A. van der Hucht & B. Hidayat (Dordrecht: Kluwer), 529
Folatelli, G., Bersten, M. C., Benvenuto, O. G., et al. 2014, ApJL, 793, L22
Georgy, C. 2012, A&A, 538, L8
Georgy, C., Meynet, G., Walder, R., Folini, D., & Maeder, A. 2009, A&A, 502, 611
Gilkis, A., & Arcavi, I. 2022, MNRAS, 511, 691
Gilkis, A., Vink, J. S., Eldridge, J. J., & Tout, C. A. 2019, MNRAS, 486, 4451
Götberg, Y., de Mink, S. E., & Groh, J. H. 2017, A&A, 608, A11
Groh, J. H., Meynet, G., & Ekström, S. 2013, A&A, 550, L7
Heger, A., Fryer, C. L., Woosley, S. E., Langer, N., & Hartmann, D. H. 2003, ApJ, 591, 288
Heger, A., Langer, N., & Woosley, S. E. 2000, ApJ, 528, 368
Iglesias, C. A., & Rogers, F. J. 1996, ApJ, 464, 943
Joss, P. C., Podsiadlowski, P., Hsu, J. J. L., & Rappaport, S. 1988, Natur, 331, 237
Langer, N. 1998, A&A, 329, 551
Limongi, M., & Chieffi, A. 2009, MmSAI, 80, 151
Limongi, M., & Chieffi, A. 2018, ApJS, 237, 13
Lohev, N., Sabach, E., Gilkis, A., & Soker, N. 2019, MNRAS, 490, 9
Lyman, J. D., Levan, A. J., James, P. A., et al. 2016, MNRAS, 458, 1768
Maeda, K., Hattori, T., Milisavljevic, D., et al. 2015, ApJ, 807, 35
Maeder, A., & Meynet, G. 1987, A&A, 182, 243
Maeder, A., & Meynet, G. 2000a, A&A, 361, 159
Maeder, A., & Meynet, G. 2000b, ARA&A, 38, 143
Maeder, A., & Meynet, G. 2012, RvMP, 84, 25
Maeder, A., & Meynet, G. 2014, ApJ, 793, 123
Maeder, A., Meynet, G., Ekström, S., & Georgy, C. 2009, CoAst, 158, 72
Markova, N., Puls, J., & Langer, N. 2018, A&A, 613, A12
Maund, J. R. 2018, MNRAS, 476, 2629
Maund, J. R. 2019, ApJ, 883, 86
Maund, J. R., Smartt, S. J., Kudritzki, R. P., Podsiadlowski, P., & Gilmore, G. F. 2004, Natur, 427, 129
Meynet, G., Chomienne, V., Ekström, S., et al. 2015, A&A, 575, A60
Meynet, G., & Maeder, A. 2000, A&A, 361, 101
Meynet, G., & Maeder, A. 2003, A&A, 404, 975
Nomoto, K., Filippenko, A. V., & Shigeyama, T. 1990, A&A, 240, L1
Nomoto, K., Suzuki, T., Shigeyama, T., et al. 1993, Natur, 364, 507
Nugis, T., & Lamers, H. J. G. L. M. 2000, A&A, 360, 227
Ouchi, R., & Maeda, K. 2017, ApJ, 840, 90
Paxton, B., Bildsten, L., Dotter, A., et al. 2011, ApJS, 192, 3
Paxton, B., Cantiello, M., Arras, P., et al. 2013, ApJS, 208, 4
Paxton, B., Marchant, P., Schwab, J., et al. 2015, ApJS, 220, 15
Paxton, B., Schwab, J., Bauer, E. B., et al. 2018, ApJS, 234, 34
Peimbert, M., Luridiana, V., & Peimbert, A. 2007, ApJ, 666, 636
Pinsonneault, M. H., Kawaler, S. D., Sofia, S., & Demarque, P. 1989, ApJ, 338, 424
Podsiadlowski, P., Hsu, J. J. L., Joss, P. C., & Ross, R. R. 1993, Natur, 364, 509
Podsiadlowski, P., Joss, P. C., & Hsu, J. J. L. 1992, ApJ, 391, 246
Prentice, S. J., Ashall, C., James, P. A., et al. 2019, MNRAS, 485, 1559
Ritter, H. 1988, A&A, 202, 93
Ryder, S. D., Van Dyk, S. D., Fox, O. D., et al. 2018, ApJ, 856, 83
Sana, H., de Mink, S. E., de Koter, A., et al. 2012, Sci, 337, 444
Schmidt, B. P., Kirshner, R. P., Eastman, R. G., et al. 1993, Natur, 364, 600
Soker, N. 2017, MNRAS, 470, L102
Song, H. F., Meynet, G., Maeder, A., et al. 2018, A&A, 609, A3
Song, H. F., Meynet, G., Maeder, A., Ekström, S., & Eggenberger, P. 2016, A&A, 585, A120
Sravan, N., Marchant, P., Kalogera, V., & Margutti, R. 2018, ApJL, 852, L17

Sravan, N., Marchant, P., Kalogera, V., Milisavljevic, D., & Margutti, R. 2020, ApJ, 903, 70
Stancliffe, R. J., & Eldridge, J. J. 2009, MNRAS, 396, 1699
Stancliffe, R. J., Fossati, L., Passy, J. C., & Schneider, F. R. N. 2015, A&A, 575, A117
Strotjohann, N. L., Ofek, E. O., Gal-Yam, A., et al. 2015, ApJ, 811, 117
Sukhbold, T., & Woosley, S. E. 2014, ApJ, 783, 10
Taddia, F., Lunnan, R., Sollerman, J., et al. 2018, Transient Name Server Discovery Report, 2018-548
Torrey, P., Vogelsberger, M., Marinacci, F., et al. 2019, MNRAS, 484, 5587
van, S., & van der Veen, A. J. 2005, ITSP, 53, 896
Vink, J. S. 2017, A&A, 607, L8
Vink, J. S., de Koter, A., & Lamers, H. J. G. L. M. 2000, A&A, 362, 295
Vink, J. S., de Koter, A., & Lamers, H. J. G. L. M. 2001, A&A, 369, 574
Vink, J. S., & Sander, A. A. C. 2021, MNRAS, 504, 2051
Wellstein, S., Langer, N., & Braun, H. 2001, A&A, 369, 939
Woosley, S. E., Eastman, R. G., Weaver, T. A., & Pinto, P. A. 1994, ApJ, 429, 300
Woosley, S. E., Langer, N., & Weaver, T. A. 1993, ApJ, 411, 823
Yoon, S.-C. 2015, PASA, 32, e015
Yoon, S.-C., Dessart, L., & Clocchiatti, A. 2017, ApJ, 840, 10
Yoon, S. C., Langer, N., & Norman, C. 2006, A&A, 460, 199
Yoon, S. C., Woosley, S. E., & Langer, N. 2010, ApJ, 725, 940